Marine Hydrokinetic Power Plant:
Software Simulation for Voltage Flicker Mitigation

by

Sang Won Seo

A thesis submitted to the Graduate Faculty of
Auburn University
in partial fulfillment of the
requirements for the Degree of
Master of Science

Auburn, Alabama
August 8, 2020

Keywords: tidal and river power, marine hydrokinetic power,
voltage flicker, power simulation model, renewable energy

Approved by

Eduard Muljadi, Chair, Professor of Electrical and Computer Engineering
R. Mark Nelms, Department Chair Professor of Electrical and Computer Engineering
Mark Halpin, Alabama Power Company Professor of Electrical and Computer Engineering

Abstract

In a marine hydrokinetic (MHK) power generation such as a tidal and river power generation, the nature of water flow (i.e., water turbulence) and the grid condition can induce voltage fluctuations or flicker at the power grid. Voltage flicker can be a serious power quality issue that can limit the integration of the MHK power plant into the utility grid. Hence, the assessment of flicker and methods to alleviate flicker are required to implement the MHK power generation. This thesis investigates the effectiveness of three different techniques for flicker mitigation by comparing the short-term flicker level and determines the appropriate mitigation technique based on the grid condition and water turbulence intensity throughout the digital simulation. The case study is performed by the digital simulation tool of PSCAD/EMTDC, modelling the MHK power generation. Then, the hardware simulation will verify the results in the software simulation as future work.

Acknowledgments

I express my special gratitude to my advisors, Professor Eduard Muljadi and Dr. Jinho Kim who have taught, guided, and inspired me to accomplish my academic career during my master's degree. I also would like to thank Professor R. Mark Nelms for his support and encouragement and Professor Mark Halpin for the knowledge that I can obtain from his many lectures.

Lastly, I specially thank my family members, colleagues in the power team, and my beloved one, Jane Ahn, in so many ways.

Table of Contents

List of Tables

List of Figures

List of Abbreviations

MHK	Marine Hydrokinetic
IEA	International Energy Agency
SCR	Short Circuit Ratio
BESS	Battery Energy Storage System
ESS	Energy Storage System
MSC	Machine Side Converter
GSC	Grid Side Converter
PCC	Point of Common Coupling
VAR	Reactive power
MPPT	Maximum Power Point Tracking
IEC	International Electrotechnical Commission
PMSG	Permanent Magnet Synchronous Generator
IGBT	Insulated-Gate Bipolar Transistor
ORPC	Ocean Renewable Power Company
EMF	Electromagnetic Field
SOC	State of Charge
VFD	Variable Frequency Drive

1. Introduction

1.1 Trend of Renewable Energy and Marine Hydrokinetic Power Generation

During recent decades, the integration of renewable power generation has become globally popular due to the many environmental concerns and rapid decreases in fossil fuels [1]. Many types of renewable generation have been developed and are commercially viable and even economically competitive, including wind, solar power, and new types of renewable resources such as the MHK power generation (e.g., tidal and river power generation) [2].

In addition, fossil fuels fundamentally give worldwide energy necessities. In 2017, the energy shares worldwide from fossil fuel was 77.4% of the whole essential energy utilization. This essential energy utilization comprises of 30.3% of petroleum, 21.2% of natural gas, 25.9% of coal, 9.1% of biofuels and waste, 4.1% of nuclear, 6.5% hydroelectricity, 2.9% of renewable energy such as wind, solar, or other renewable sources based on International Energy Agency (IEA) [3]. The result of the reliance on fossil fuels is getting to be progressively concerning, and the environmental problem of the abuse of burning fossil fuels causes the excessive CO_2 to discharge, limiting the soil to emanate the warm from the Sun and increasing worldwide issues known as the greenhouse impact. Therefore, the renewable energy sources and their development become one of the solutions that can reduce environmental issues and decrease the abuse of fossil fuels to spare them for the future. Hence, the integration and study of renewable power generations have expanded from wind and solar power to new types of renewable applications such as the MHK power generation, including the river and tidal power generation [2].

The MHK power generation is an economically viable renewable energy source and a long-standing and reliable technology [4]. The hydrokinetic power plant is invented to overcome the drawbacks of the traditional hydropower generation, which is associated with building a dam, so that the MHK power generation in the river or sea does not interfere with the nearby environment and habitats and change the water flow direction. In the MHK power generation, the input resources are more predictable and slower, but also steadier than in wind and solar generation even though the level of water turbulence may still vary from one place to another [2]. River and tidal energy sources can be easily predicted from the gravitational and centrifugal forces between the Earth and the Moon, so the high and low tides are expected by well-known cycles or measurement of the water flow in the regional area [5].

The MHK power generation requires the appropriate technical design based on the environmental conditions and power system conditions. It depends on water flow characteristics, types of the hydrokinetic turbine, and the condition of the power system in the specific area. In addition to it, as the development of the MHK power generation and power electronic devices escalates rapidly, power conversion, power quality, and reliability have become more important in the hydrokinetic power industry. Therefore, the influence of MHK turbines on power quality should be regarded as an important issue.

The integration of renewable power generation still faces its power quality issue because of the intermittent nature of energy and the high penetration of energy. Thus, the power quality issues such as voltage flicker, voltage unbalance, or harmonics should be resolved to satisfy the grid codes and technical requirement guaranteeing good quality of power when integrating the renewable power plant to the utility grid.

1.2 Hydrokinetic Energy from Tide

There are two types of the hydrokinetic energy conversion in the water flow driving the hydrokinetic turbine: one utilizes the tidal barrage that uses the difference of the water flow between the high and low tide, and the other utilizes the water flow during the flood and ebb of the water. In the tidal hydrokinetic energy, the water flows have two ways because of the flood and ebb based on the tidal cycles. In the river power generation, the river current flows that drive the hydrokinetic turbine are in one direction, so it does not require the reversible turbine.

The sea or river tides routinely rise and fall based on the gravitational force between the Earth and Moon. Tides are long-period waves that move through the oceans in response to the gravitational forces exerted by the Moon and Sun. Tides start within the oceans and advance toward the coastlines where they appear as the regular rise and fall of the sea surface. The difference between high tide and low tide is called the tidal range. A horizontal movement of water often regularly goes with the rising and falling of the tide; this is called the tidal current [6]. The approaching tide along the coast and into the shore is called a flood current, and the outgoing tide is called an ebb current. The strongest flood and ebb currents usually occur before or close to when the high and low tides occur. Within the open ocean, tidal currents are moderately weak; on the other hand, within the close estuary passages or narrow straits and inlets, the speed of the tidal current is relatively fast than the previous situation. Figure 1.1 demonstrates the diagram of the tidal ranges and ebb and flood current movement, as explained above. Therefore, the places where the MHK power plant is installed determines the water flow characteristics, such as the water flow speed or the turbulence intensity of water stream.

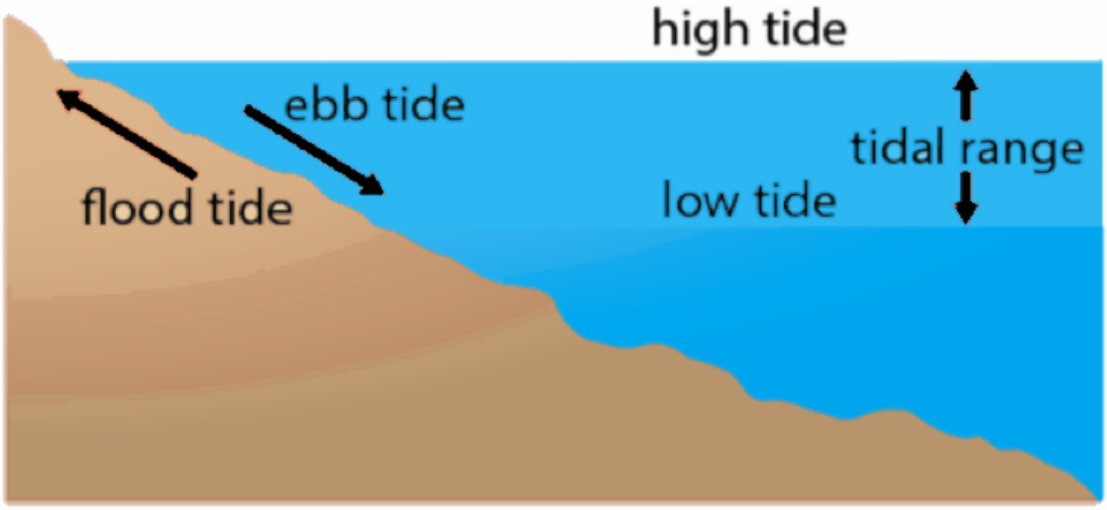

Figure 1.1. Tidal range and ebb and flood current

Gravity is one major force that induces tides. Tides are caused by the gravitational pull of the Sun and the Moon on the Earth's water [6]. In Figure 1.2, when the Sun, Moon, and Earth are on a straight line (left), tides are higher and lower than usual; in contrast, when the lines between the Sun and Earth and the Moon and Earth are perpendicular to one another (right), high tides and low tides are moderated [6]. Tides are created through a combination of forces applied by the gravitational pull of the Sun and the Moon and the revolution of the Earth.

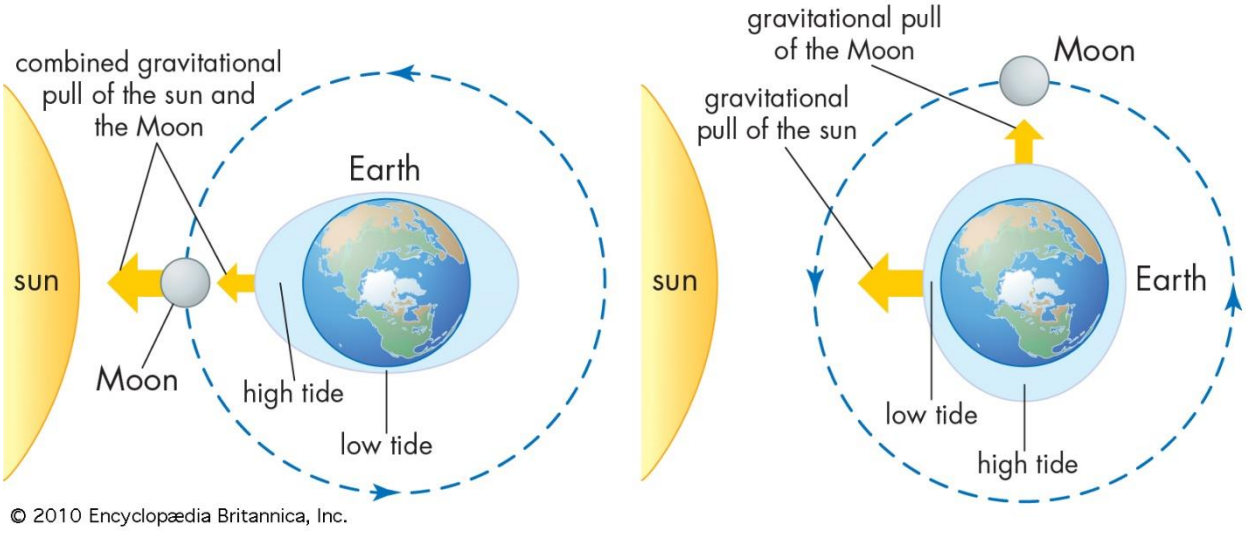

Figure 1.2. Tide and the gravitational force of the Sun, Moon, and Earth [6]

The relative movement of the three bodies produces different tidal cycles that influence the range of the tides [7]. However, since the Moon and Sun movement are regular – two high tides and two low tides within the day, the tidal hydrokinetic energy is more predictable and stable than other renewable energy sources such as wind or solar. Hence, the MHK power generation might take advantage of the less variation in the energy intensity over other renewable energy sources.

This section intends to present the characteristics of the tidal and river power generation; compared to wind power, the hydrokinetic power has a relatively lower speed of the water flow. But, the MHK energy has a higher density than air, making hydrokinetic energy conceivable to create enough power at even low speeds. However, there is still a nontrivial drawback in the hydrokinetic energy characteristics such as varying water speed and water turbulence; the hydrokinetic power generation can cause the short-term voltage noises to the grid utility called "voltage flicker" because of this variable speed of water flow.

1.3 Voltage Flicker in the MHK Power Generation

According to the IEEE standard [8], voltage fluctuation is defined as a series of voltage changes or cyclical variations of the voltage envelope. Voltage fluctuation is often caused by the variability of the voltage drop across the line impedance when delivering the variable generations or variable loads. The unsteady voltage at the grid sometimes causes perceptible illumination changes from lighting equipment [8]. These luminous fluctuations occurred at low frequency (i.e., 8-10 Hz, usually). It can be subjectively perceived by human eyes and irritate some customers. This power quality issue is referred to as flicker, and flicker occurs when the frequency of observed variation lies between a few hertz [9]. Therefore, the voltage flicker is short-term variation in voltage, and its example graph is shown in Figure 1.3 [10]. In the literature [10], the description of flicker and its phenomenon is thoroughly explained.

To assess flicker perception caused by voltage fluctuations and to calculate the short-term flicker severity P_{st}, a flickermeter model is specified by the IEC standard IEC 61000-4-5 [11]. Flickermeter is designed to transform the fluctuating input voltage into the statistically analyzed parameter related to flicker perception. This process implements the process of visual perception, which is a lamp-eye-brain chain [11]; the UIE/IEC flickermeter consists of five blocks, and the block diagram is shown in Figure. 1.4. The simulation model of flickermeter is developed in MATLAB/SIMULINK based on the IEC standard IEC 61000-4-5. The results of grid voltage from PSCAD simulation are transferred to MATLAB/SIMULINK flickermeter simulation. Then, flickermeter calculates P_{st} to objectively assess voltage fluctuations from the simulation results in PSCAD simulation of the MHK power generation.

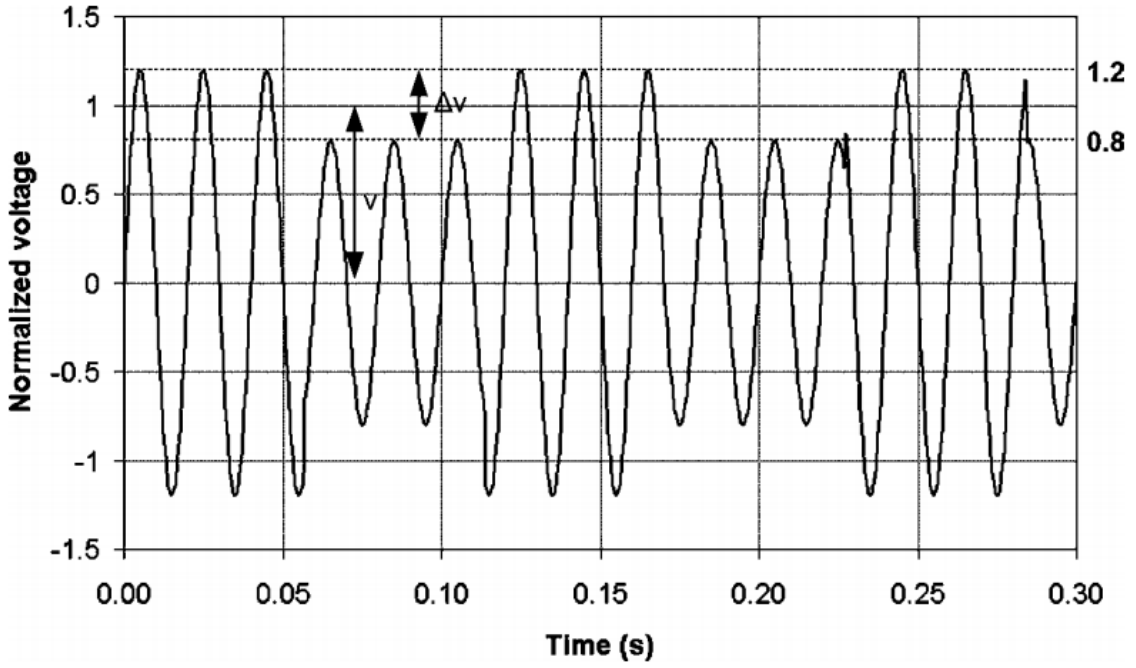

Figure 1.3. Example of voltage flicker [11].

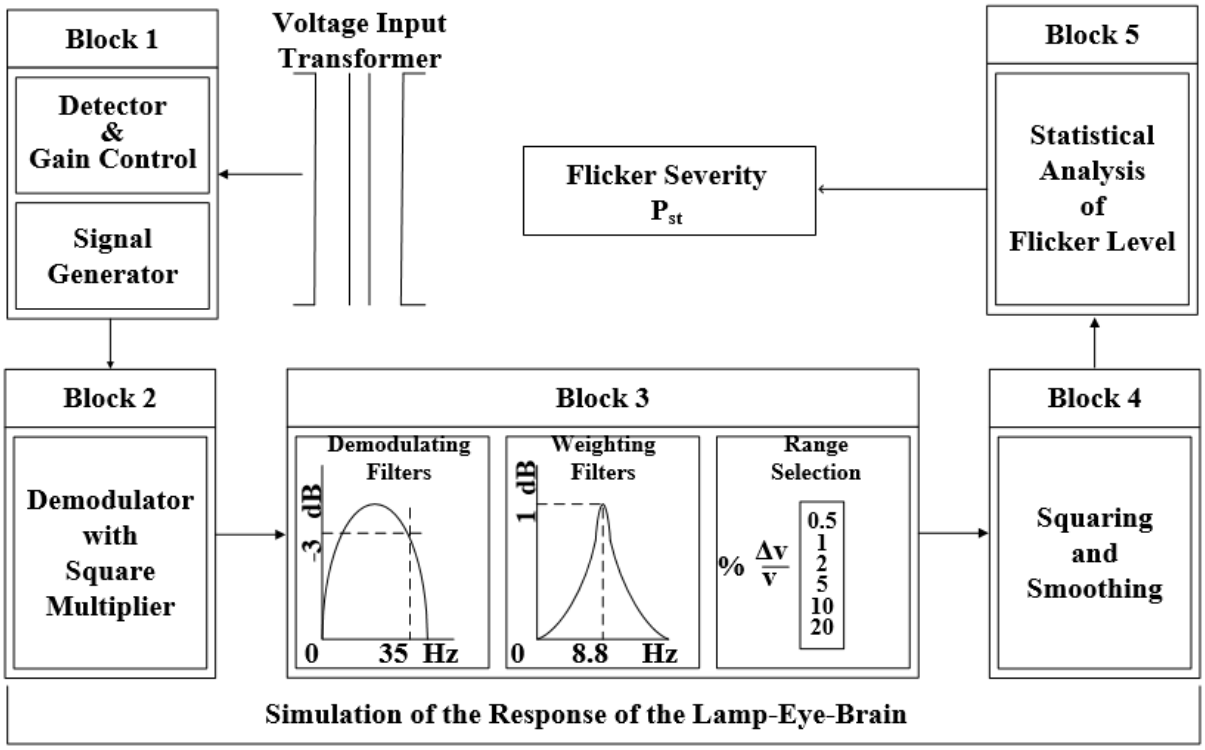

Figure 1.4. Flickermeter diagram.

In block 1 in flickermeter, the input voltage adapter scales the input voltages to the internal reference value, and it emulates a characteristic of the human perception in a moderate-level. Block 2 uses a quadratic demodulator to square the scaled input and separates the voltage fluctuation from the main voltage signal. Block 2, hence, simulates the behavior of an incandescent lamp. Block 3 consists of two filters that remove the values which have frequencies higher than that of the supply voltage and DC component, generated from block 2. Demodulating filter in block 3 incorporates a first-order high-pass filter at 0.05 Hz cutoff frequency and sixth-order low-pass Butterworth at 35 Hz, and the weighting filter gives a band-pass response centered at 8.8 Hz which simulates the response of the human eye to the sinusoidal voltage fluctuation of the lamp [12]. Block 4 emulates the memory tendency of the human brain within the time constant of 300 ms, throughout the squaring and smoothing filters. The output from

block 4 represents the instantaneous flicker level. Block 5 performs the statistical analysis throughout the statistical classification to express the cumulative probability of flicker sensation. From the output of the previous block (instantaneous flicker level), the classifier calculates the short-term flicker severity index (P_{st}) for 10 minutes and the long-term flicker severity index (P_{lt}) for 2 hours. The case study in this thesis only calculates P_{st} because of the simulation time. The equation of P_{st} is defined as:

$$P_{st} = \sqrt{0.0314P_{0.1} + 0.0525P_{1s} + 0.0657P_{3s} + 0.28P_{10s} + 0.08P_{50s}} \qquad (1.1)$$

where $P_{0.1}$, P_{1s}, P_{3s}, P_{10s}, and P_{50s} are flicker levels that exceed 0.1, 1, 3, 10, and 50 percent of the time. Therefore, in block 5, flickermeter can provide the objective value on flicker severity level independently of the type of voltage fluctuation and time variation law. In the case study, flicker severities from each mitigation control scheme are compared by P_{st} of the simulation results running in 600 seconds. The explanation of each block of flickermeter is excerpted from the IEC standard IEC 61000-4-5 [11].

Therefore, flicker caused by the voltage fluctuations might be considered a limiting factor of the integration of the MHK power generation in some specific grid conditions. Flicker emission of the MHK power generation is mainly induced by two factors, such as the variable speed of the hydrokinetic turbine and grid conditions. The hydrokinetic energy characteristics such as water turbulence and variable water speed will cause the power fluctuation to the hydrokinetic turbine and affect the voltage fluctuation to the grid utility. In addition to the power source condition, the grid conditions that vary by short-circuit ratio (SCR) and grid impedance angle also impact flicker emissions [13].

The input resource from the tidal and river power generation is more predictable and less fluctuating than the wind or other renewable power sources. However, the water speed is still varying because of the water turbulence (chaotic water movement) that may cause flicker emission on the grid in the tidal and river power generation. According to [13], increasing turbulence strength with the increasing mean speed of hydrokinetic turbine mainly causes an increase in flicker level. Turbulence intensity measured in the upstream and downstream of a turbine determines the turbulence strength of the water flow and quantifies the turbulence [14]. The turbulence intensity is defined as:

$$\mathrm{TI}\% = \frac{\sqrt{\sum_{i=1}^{N} \frac{(U_i - \bar{U})^2}{N}}}{\bar{U}} \times 100 \qquad (1.2)$$

where U_i the *i*th instantaneous velocity measurement or local oscillations, $\bar{U}$ is the mean velocity of the water stream in $\mathrm{m/s}$, and N the number of measurement points. Figure 1.5 demonstrates the turbulence in fluid dynamics. In the software simulation, the turbulence intensity indicates the severity of the water turbulence, and the water turbulence is generated by the random noise generation with the mean water speed. Then, the turbulence intensity in the equation (1.2) is calculated from the simulation's obtained water flow speed. Therefore, the variable water speed caused by the water turbulence induces the power fluctuation to the hydrokinetic turbine, and it will cause the voltage flicker to the grid.

It is very important to assess the voltage flickers in the MHK power generation and resolve the voltage fluctuation with the proposed control so that the implementation of the MHK power generation guarantees the stabilized power system and provides good power quality to customers. The integration of the hydrokinetic should regard the condition of the power system

where the tidal generation is deployed, and proper controls for mitigating the voltage fluctuation should be implemented into the system.

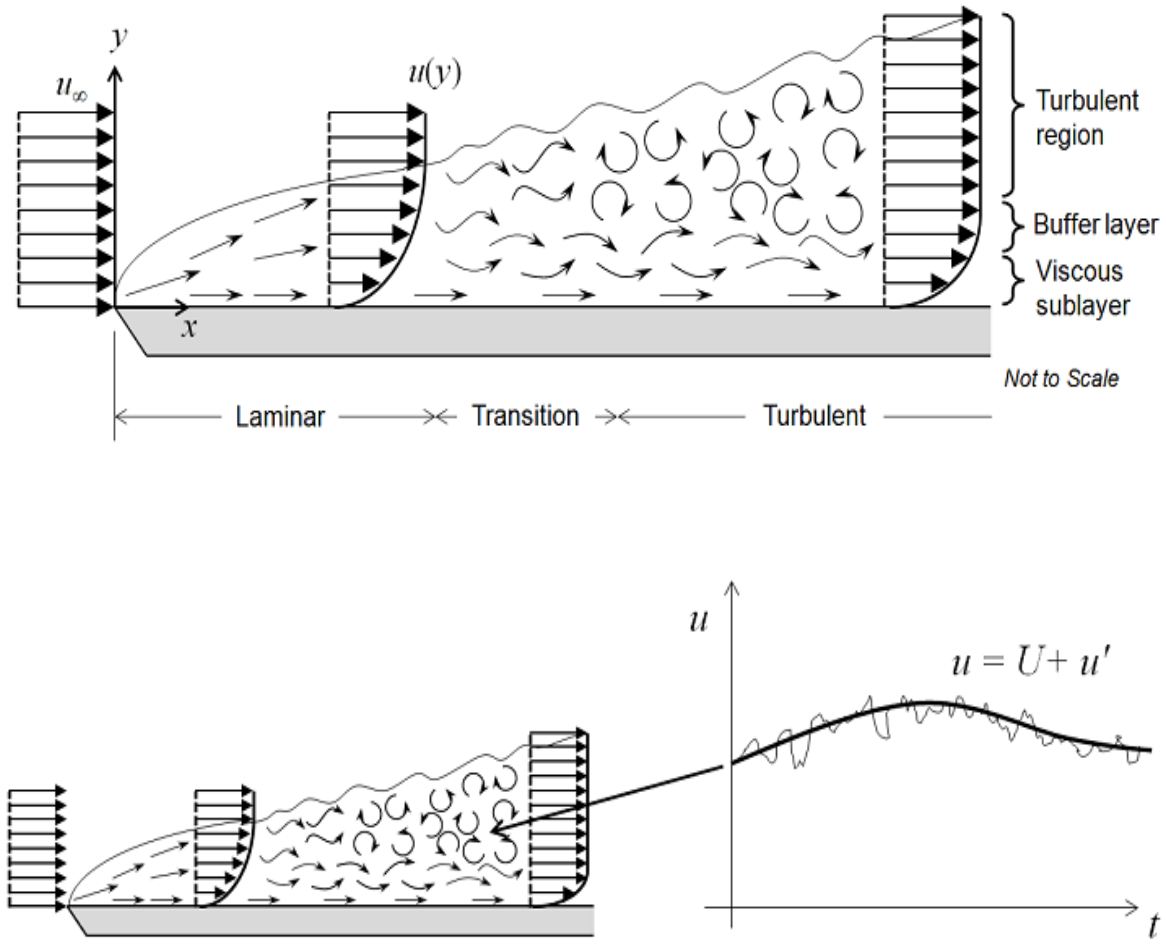

Figure 1.5. Water turbulence and fluid dynamics

1.4 Flicker Mitigation Techniques and Proposal

The study of flicker mitigation in wind power system are proposed more than in the MHK power system. Still, the essential objective for flicker mitigation in the variable energy sources is same: reduction on voltage fluctuation and service of better power quality. Many solutions to mitigate flicker of renewable power generation (e.g., wind power) by using active power smoothing such as energy storage system (ESS), a supercapacitor, or active power curtailment has been proposed in [15] - [17]; however, these solutions that smooth the active power fluctuation from the source require the deployment of external equipment due to the implementation of the dedicated storage to the power system and a financial burden [18].

Therefore, the other cost-effective and popular technique to mitigate flicker in renewable power generation is the reactive power compensation which can be accomplished by the VAR control on the grid side converter (GSC) of the renewable power generation or by a separate STATCOM at the point of common coupling (PCC) [18], [19]. Yet, these reactive power compensation techniques also have shortcomings and limitations in a certain situation. STATCOM may effectively mitigate flicker by stabilizing the power transient and compensating a large amount of the reactive power; however, it needs closer control integration with the power converter to respond within 1-25 Hz and is not financially viable for distribution network [18]. The VAR control on the GSC in the power conversion system would be financially viable and effectively implemented with the power converter; however, the VAR control has a limit to efficiently mitigate the voltage fluctuation occurred in the low X/R ratios and low short circuit ratio (SCR). The voltage fluctuation in the distribution network with the low X/R ratio is dominant to the real power fluctuation. Besides, there is the operating limit to control the reactive power in the GSC because of the capacity of the converter (i.e., the current limit of the

power electronic switches and high communication frequency) [20]. The reactive power delivery is limited by the amount of the apparent power of the power converter.

Hence, to overcome the limitation of the VAR control on the GSC, this study also suggests using the Battery Energy Storage System (BESS) for flicker mitigation in the case of the low grid impedance angle and distribution network, even though it is financially inferior to the VAR control. As shown later, the limited size of the BESS can be used to sufficiently mitigate flicker even in the low X/R ratio by preventing the real power fluctuation from the generator. In essence, the BESS control system delivers the average (smooth) power output from the hydrokinetic turbine to the grid while keeping the turbulent (low harmonics) power in and out of the BESS; however, the BESS is still considered to be less financially viable and might not have enough space to deploy the external equipment and dedicated storage.

If both VAR control and BESS control are limited by technical and economical design in the project, then the adaptive control by injecting the different reactive powers with the $I_q - V_{grid}$ adaptive control scheme implemented in the GSC can be used to effectively mitigate flicker. Based on the I_q capability of the system that is determined by the size of the converter and the limit of voltage fluctuation magnitude at the PCC, the control gain for the GSC controller will be varied adaptively. It can also determine the amount of the reactive power injected into the system and minimize the voltage fluctuation at the distribution network with the fast control response.

This thesis proposes an analysis of three different techniques to mitigate flicker in the MHK power plant: the VAR control in the GSC, the use of the BESS, and the adaptive control of reactive power injection in the GSC. Their impacts on flicker mitigation in different grid conditions and water turbulence are analyzed throughout the case study. Hence, the results in the case study examine the operational limits of each control even in a distribution network with the

low X/R ratio and very severe water turbulence, so it determines which techniques are required to be used for flicker mitigation by comparing the quantified measurement of flicker severities throughout the case study. The dynamic model of the grid-connected MHK power generation is developed in the simulation tool of PSCAD/EMTDC. Simulation results from the case study will verify the feasibility of each technique and its effectiveness on flicker mitigation. In this thesis, the terms of the MHK power generation, hydrokinetic power generation, and tidal and river power generation might be used interchangeably, but each term shares the same expression.

Furthermore, the hardware design of the MHK power system consisting of the variable speed motor that depicts the hydrokinetic turbine, the synchronous generator, and the power converters connected to grid simulation will be designed to verify results of the digital simulation of the MHK power generation. The hardware design for the verification of the digital simulation will be discussed in Appendix 1, considering it as future work.

2. Theoretical Model of MHK Power Generation for Digital Simulation

2.1 Description of Electrical Conversion of MHK Power Generation in System Level

The MHK power generation takes the hydrokinetic energy from the hydrokinetic turbine, and the hydrokinetic turbine drives the permanent magnet synchronous generator (PMSG) to generate the electrical powers. The back-to-back power converter with the corresponding control scheme suggested in [2], [21] is used to deliver the constant AC power to the grid because of the lack of a field winding and nature of the variable power out of the PMSG driven by the turbine. To summarize the electrical conversion of the MHK power generation, the major processes of the electrical conversion from the hydrokinetic turbine to the grid are as follow [2], [21]:

1. Hydrokinetic energy from the hydrokinetic turbine is converted into the electrical power by the PMSG
2. The variable AC power out of the PMSG is converted into the variable DC voltage throughout the three-phase diode rectifier.
3. The variable DC voltage out of the diode bridge is passed through the DC-DC boost converter, and the DC-DC boost converter can deliver maximum C_p operation to maximize power generation from the turbine.

4. The DC-AC inverter in the GSC converts DC voltage at DC bus into the three-phase AC voltage at 60 Hz and maintains the DC bus voltage constant by its implemented control scheme.

The configuration of the grid-connected tidal power generation used in the digital simulation is shown in Figure 2.1. The control tasks of the hydrokinetic turbine and the power converters in the digital simulation will be discussed in Chapters 2.3 and 2.4.

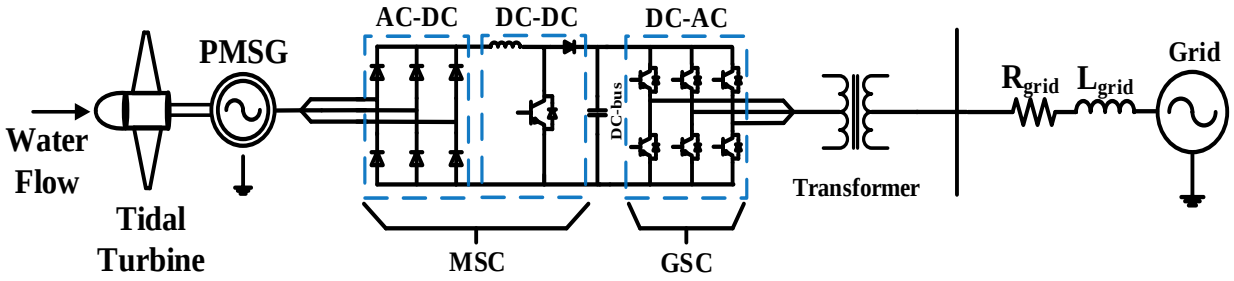

Figure 2.1. Configuration of grid-connected MHK power generation

For the description of the back-to-back converter shown in Figure 2.1, the Machine Side Converter (MSC) includes the three-phase diode rectifier and DC-DC boost converter and the Grid Side Converter (GSC) represents the DC-AC inverter that is consisted of IGBTs. The simulation and modeling for each electrical component are performed by the dynamic power system simulation, PSCAD.

2.2 Hydrokinetic Turbine

There are two major types of the hydrokinetic prime mover (hydrokinetic turbine in this project) in the river and tidal power generation: horizontal axis type and vertical axis type of the hydrokinetic turbine, as shown in Figure 2.2 [22]. The type of the hydrokinetic turbine is determined by the energy resources (e.g., direction of the water flow) and sites (e.g., available spaces in the water). As shown in Figure 2.2, the horizontal axis hydrokinetic turbine works and

looks very similar to the conventional wind turbine; the rotational axis of the rotor is parallel to the water stream, and it can be mounted on the seabed or floating structure mounted (Buoyant) [22]. The vertical axis hydrokinetic turbines shown in Figure 2.2 have different designs of blades, but the basic working principles of these are the same; the rotational axis of the rotor is perpendicular to the water stream, and they have the design simplicity. The details in the reviews of the hydrokinetic turbine types and their comparative analysis are thoroughly explained in the literature [22]. In the digital simulation for this thesis, the hydrokinetic prime mover is assumed to be a series of Gorlov hydrokinetic power generation [23], and the parameters for the turbine are used as specified in [2] [28]. As shown in Figure 2.3, the Gorlov hydrokinetic power generation consists of two connected sets of the turbines driving the generator in the middle.

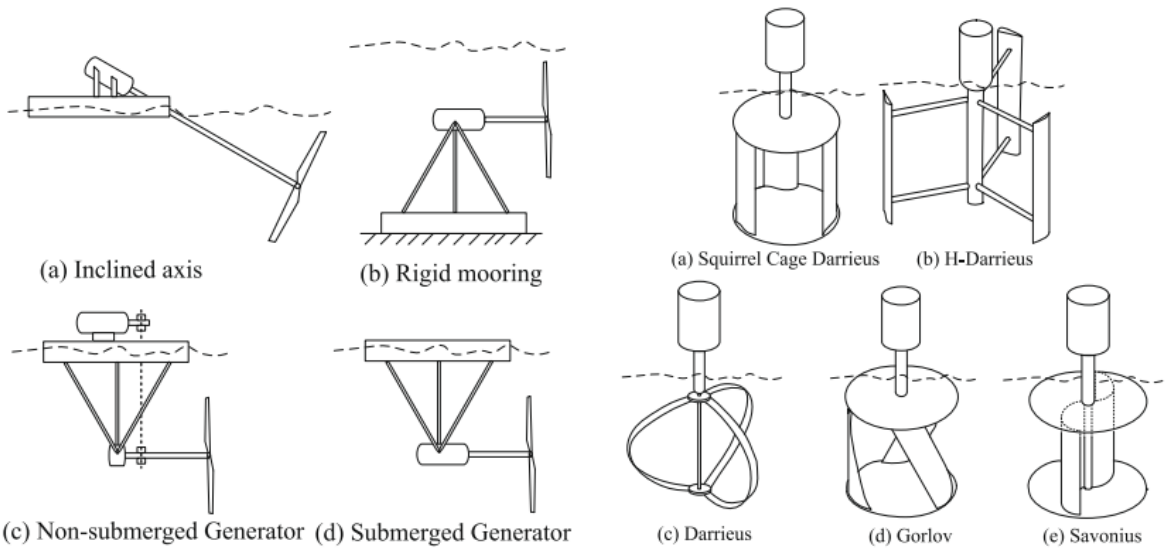

Figure 2.2. Examples of the hydrokinetic turbine types [22].

Figure 2.3. ORPC series-connected Gorlov turbine [23]

2.3 PMSG and Control of Generator with MPPT

As mentioned previously, the electrical power in the tidal power generation is induced by the PMSG that is directly driven by the hydrokinetic turbine. The PMSG is a synchronous generator whose excitation field is provided by the permanent magnet. The PMSG has the advantage of higher efficiency due to high flux density and the reliability for a long-term application (low maintenance cost), and it can be operated even at low speeds without the gearbox, still showing good performance [24]. Therefore, the digital simulation model of the MHK power generation in this thesis uses the PMSG as the power generator, considering the advantages of implementation in the system (e.g., small and light generator mounted on the hydrokinetic turbine apparatus, high efficiency, high reliability, low-speed operation). However, since the PMSG lacks field winding and the nature of variable generation, the PMSG shall require the back-to-back converter to provide the regulated voltage to the grid [2]. In this chapter, the mathematical model of the PMSG is described, and the control of the hydrokinetic turbine with the Maximum Power Point Tracking (MPPT) is presented.

In the PMSG operation, the frequency of the induced voltage in the stator is directly proportional to the rotor speed (it can be expressed in RPM or rad/s) as follows:

$$RPM = 120 * \frac{f_s}{n_P} \ [RPM] \tag{2.1}$$

$$\omega_G = RPM * 2 * \frac{\pi}{60} \left[\frac{rad}{s}\right] \tag{2.2}$$

where f_s is the frequency of the induced voltage in the stator, n_P is the number of the poles.

To simplify the system equations for understanding the mathematical structure and mechanism of the PMSG, the rotating transformation in the d-q frame and corresponding equations shall be explained.

The rotating coordinate system in the d-q frame is the transformation of the coordinates of the three-phase stationary coordinate system (a-b-c) to the rotating coordinate system (d-q-0); It helps define the new set of the stator variable of the generator, such as the voltages, currents, and flux in terms of the winding variables [25]. These new quantities are obtained from the projection of the actual variables in three axes: d-axis, called the direct axis, represents the direct axis of the field winding of the generator, q-axis, called the quadrature axis, represents the neutral axis of the field winding, and the stationary axis, 0-axis [25]. In Park transformation, the transformation of the coordinate system of two stationary system (α- β) can be expressed to two time-invariant coordinate systems into the d-q rotating system, and it is oriented with the real axis (d-axis) in the direction of the magnetic flux orientation as shown in Figure 2.4 [26]. In the Park transformation, the two currents in the fixed coordinate stator phase $i_{s\alpha}$ and $i_{s\beta}$ are converted into the d-q rotating currents i_{sd} and i_{sq}, as shown in Figure 2.4.

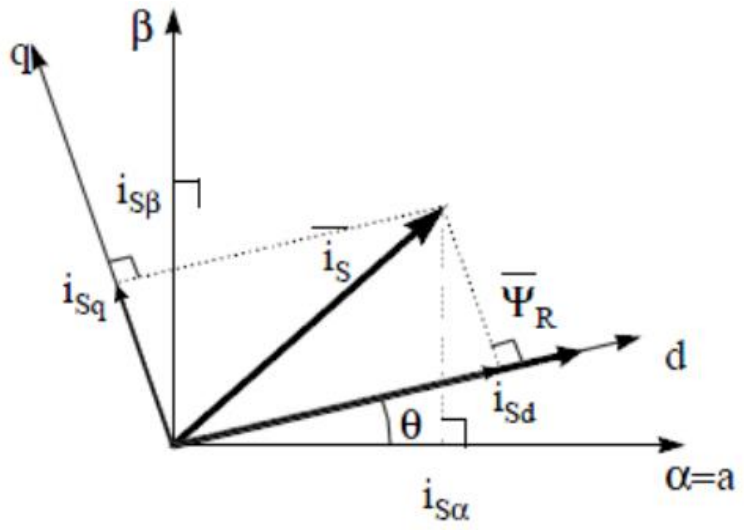

Figure 2.4. Representation of Park transformation.

The d-q-0 transformation in Park transformation is defined as the following in matrix form [26]:

$$x_{dq0} = Kx_{abc} = \sqrt{\frac{2}{3}}\begin{bmatrix} \cos(\theta_r) & \cos\left(\theta_r - \frac{2\pi}{3}\right) & \cos\left(\theta_r + \frac{2\pi}{3}\right) \\ \sin(\theta_r) & \sin\left(\theta_r - \frac{2\pi}{3}\right) & \sin\left(\theta_r + \frac{2\pi}{3}\right) \\ \frac{1}{\sqrt{2}} & \frac{1}{\sqrt{2}} & \frac{1}{\sqrt{2}} \end{bmatrix} \quad (2.3)$$

The main field-winding flux is placed along the direction of the d-axis of the rotor, and the machine EMF $\bar{E}$ goes along the rotor q-axis [26]. Then, the angle between EMF $\bar{E}$ and a terminal voltage $\bar{V}$ is the power angle δ. At t = 0, the phasor $\bar{V}$ is along with the axis of phase α as the reference axis. Therefore, the place of the d-axis of the rotor θ_r is located at $t > 0$ can be written as:

$$\theta_r = \omega_r t + \delta + \frac{\pi}{2} \quad (2.4)$$

With the concept of this transformation, the sets of voltages and currents for the PMSG modeling can be represented in the frame of d-q since the zero component can be omitted as a neutral connection.

In the frame of d-q, the instantaneous real and reactive power out of the PMSG can be written as:

$$P_{PMSG} = u_d i_d + u_q i_q \tag{2.5}$$

$$Q_{PMSG} = u_q i_d - u_d i_q \tag{2.6}$$

where u_d and u_q are the instantaneous voltage in the frame of d-axis and q-axis, and i_d and $i_q$are the instantaneous current in the frames of d-axis and q-axis, respectively.

This concept will help to understand independent control (decoupled control) of the real (d component) and reactive (q component) components in the power converter later. Therefore, the stator voltage of PMSG in the d-q frame can be given as:

$$u_{sd} = R_s i_{sd} + L_d \frac{di_{sd}}{dt} - \omega_e \Psi_{sq} \tag{2.7}$$

$$u_{sq} = R_s i_{sq} + L_q \frac{di_{sd}}{dt} + \omega_e \Psi_{sd} \tag{2.8}$$

Then, the components of the stator flux vector in the d-q frame can be given by:

$$\Psi_{sd} = L_d i_{sd} + \Psi_{PM} \tag{2.9}$$

$$\Psi_{sq} = L_q i_{sq} \tag{2.10}$$

where R_s is the stator phase resistance, L_d and $L_q$are direct and quadrature stator inductances, and Ψ_{PM} is flux established by the permanent magnets. Also, the electrical angular speed ω_e can be defined as:

$$\omega_e = n_p * \omega_G \left[\frac{rad}{s}\right] \tag{2.11}$$

where ω_G is the mechanical angular speed of the generator, and n_p is equal to the number of poles of the PMSG.

Then, the electromagnetic torque of the PMSG generator can be expressed as follows:

$$T_{em} = \frac{3}{2} n_p \left(\Psi_{sd} i_{sq} - \Psi_{sq} i_{sd} \right) \tag{2.12}$$

The mechanical equation of the rotating generator with the inertia and the rotor speed can be simplified as:

$$J \frac{d\omega_G}{dt} = T_{em} - B\omega_G - T_T \tag{2.13}$$

where J is the inertia of the PMSG, B is the friction coefficient of the PMSG, and T_T is the load torque applied to the rotating generator, which is the mechanical torque of the hydrokinetic turbine in this simulation. Therefore, the above equations representing the mathematical modeling of the PMSG are used to simulate the direct-drive PMSG used in the software design.

As mentioned previously, the hydrokinetic turbine is directly connected to the PMSG. Therefore, to present the dynamics of the hydrokinetic energy and the PMSG in the simulation, the control of the generation with the MPPT shall be discussed. In order to understand the MPPT of the hydrokinetic turbine control with the mathematical equations, the hydrokinetic power equations should be discussed. The hydrokinetic power of the hydrokinetic turbine is determined by the following equation:

$$P_{water} = 0.5 \, \rho \, A \, C_p \, V^3 \tag{2.14}$$

where ρ is the density of water, which is about 1000 [kg/m^3], A is the cross-sectional area of the turbine in [m^2], C_p is the power coefficient of the turbine, and V is the speed of the water flow in [m/s]. C_p is controlled by the ratio of the linear speed of the tip of the blade to water speed, the tip speed ratio (TSR), and its equation is defined as:

$$TSR = \frac{\omega_T R}{V} \tag{2.15}$$

where ω_T is the rotational speed of the blade, and R is the radius of the hydrokinetic turbine blade.

According to the equations (2.14) and (2.15), the C_p (power coefficient) and TSR (Tip Speed Ratio) characteristics shall be highlighted because they will determine the reference values in MPPT. The performance curve (C_p – TSR curve) of the hydrokinetic turbine in this simulation is obtained from the generic equation of the C_p – TSR curve in the literature [27], and the coefficients of the C_p – TSR curve equation are developed from the example data of the horizontal axis hydrokinetic turbine without the pitch control. The equation for the C_p – TSR curve of the hydrokinetic turbine with the fixed pitch angle (β) in this simulation is expressed as:

$$C_p(TSR, \beta) = 0.13 * \left(\frac{105}{TSR_i} - 0.9\beta - 7\right) * e^{\frac{-8.45}{TSR_i}} \quad (2.16)$$

where

$$TSR_i = 1/\left(\frac{1}{TSR + 0.001\beta} - \frac{0.8}{1 + \beta^3}\right) \quad (2.17)$$

The coefficient for the generic equation of the Cp – TSR curve can be obtained from the typical hydrokinetic turbine (horizontal axis hydrokinetic turbine with the fixed pitch angle), and description of each coefficient in the equations (2.16) and (2.17) is thoroughly explained in [27]. Based on the equation (2.16), Figure 2.5 shows the C_p – TSR curve of the hydrokinetic turbine used in the simulation.

Therefore, the MPPT for the hydrokinetic turbine keeps C_p staying at maximum as the rotational speed is changed and controls the turbine to be a stall at the low C_p region which is the left side of the C_{p_max}; this is because the pitch control is not implemented in the hydrokinetic turbine in this simulation model. The reference C_p (C_{p_max} in Figure 2.5) is corresponding to C_p^*

= 0.32, and the TSR at C_p^* is set to 2.3 as the reference values for the MPPT of the hydrokinetic turbine control [2], [27].

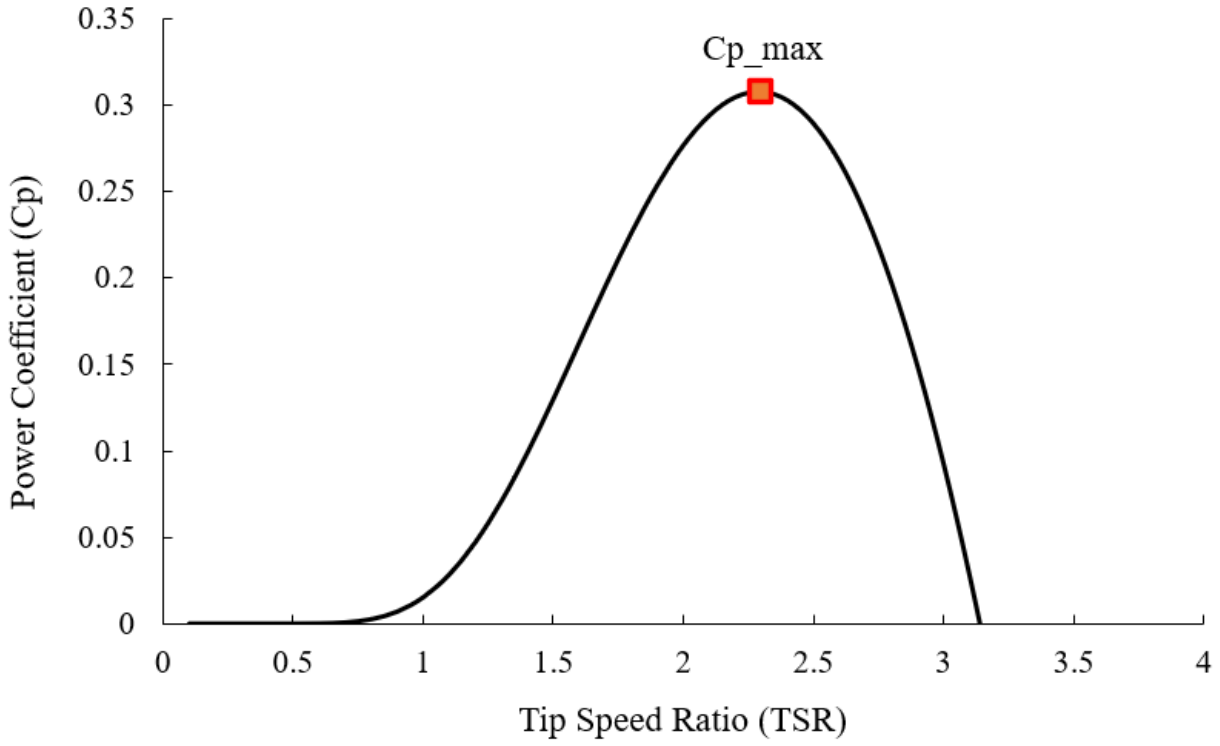

Figure 2.5. Cp and TSR curve of the hydrokinetic turbine.

Therefore, the new equation of the hydrokinetic power regarding the TSR based on the equations (2.14) and (2.15) is written as**:**

$$P_{mppt} = 0.5\,\rho\,A\,C_p^*\left(\frac{\omega_T R}{TSR^*}\right)^3 \tag{2.18}$$

where the C_p^* and the TSR^* correspond to the target C_p (C_{p_max}) and the TSR at C_p^* throughout the MPPT. Therefore, the MPPT power of the hydrokinetic turbine based on the rotational speed is rewritten as:

$$P_{mppt} = K_{cpmax} \cdot \omega_T^3 \tag{2.19}$$

To simplify the constant gain in the control of the MPPT, the proportional gain, K_{cpmax}, is defined as:

$$K_{cpmax} = 0.5\ \rho\ A\ C_p^* \left(\frac{R}{TSR^*}\right)^3 \quad (2.20)$$

In this study, hydrokinetic turbine simulation in PSCAD/EMTDC controls P_{mppt} based on the measured rotational speed of the hydrokinetic turbine ω_T; the target power (P_{mppt}) will guide the hydrokinetic turbine to operate at C_p^* as the water speed changes. Therefore, as the rotational speed is changed, the MPPT controls the hydrokinetic generator to generate the maximum power based on the reference values of C_p and TSR. In the simulation, the hydrokinetic turbine is originally operated at a water flow of 2.5 m/s (Operational between 2.0 m/s and 3.2 m/s), TSR^* is set to 2.3, C_p^* is set to 0.32, and the K_{cpmax} is set to 0.8. In the hydrokinetic turbine simulation, the tidal turbulence that is previously mentioned in the equation (1.2) is added to the water flow speed, and the turbulence intensity is set to 3.2% as a default. Therefore, the fluctuation in the real power out of the PMSG is fabricated in the simulation. The outputs of the dynamic simulation for the machine part (the hydrokinetic turbine and the PMSG) with the water turbulence that include the water flow, rotational speed, output power, and torque for both turbine and PMSG controlled by the proposed MPPT when the water flow speed gradually increases from 2.2 m/s to 3.2 m/s are shown in Figure 2.6. The mechanical equation of the shaft connecting the hydrokinetic turbine and the PMSG follows the equation (2.13).

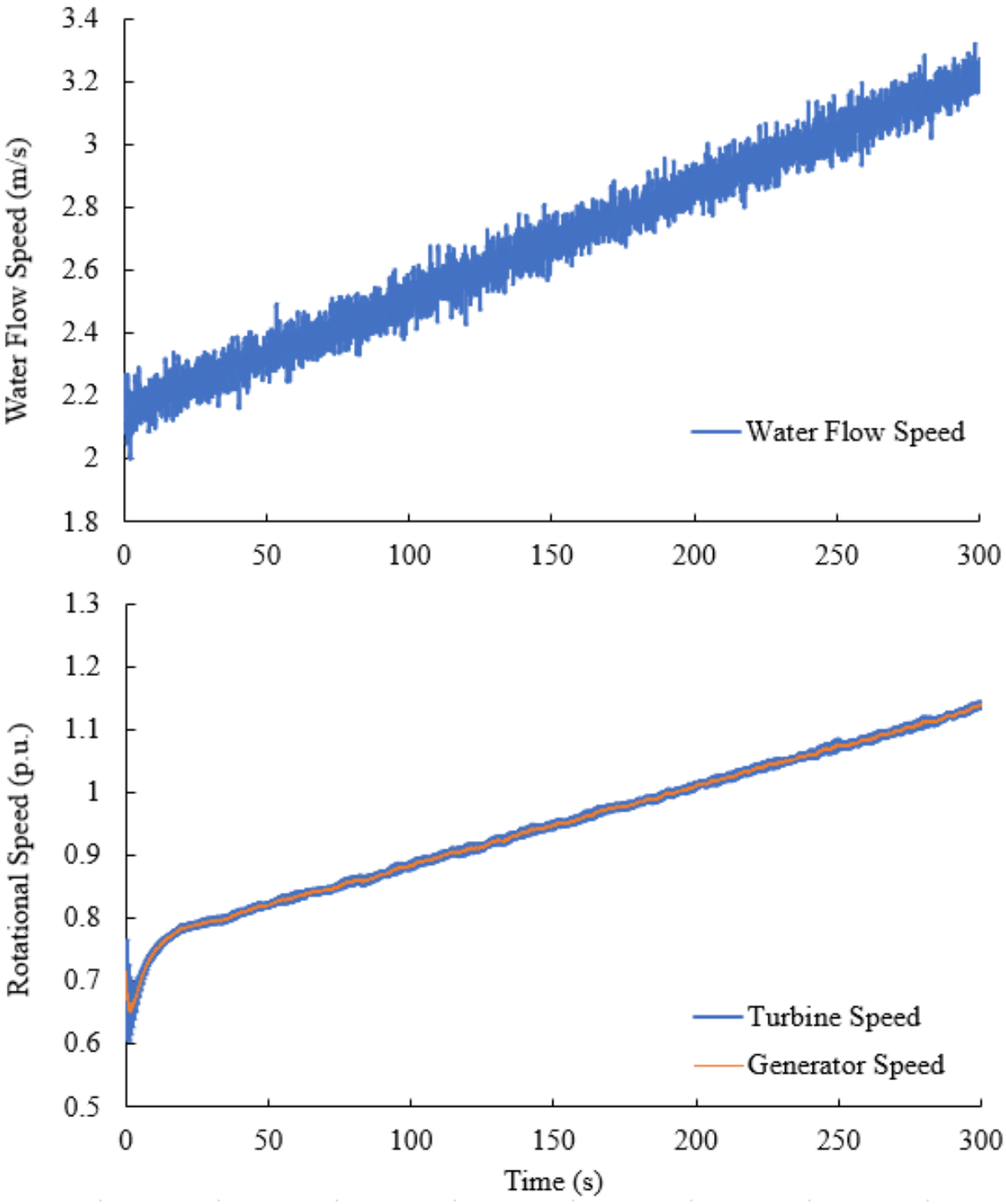

(a) Water flow speed with water turbulence and rotational speed of generator and turbine

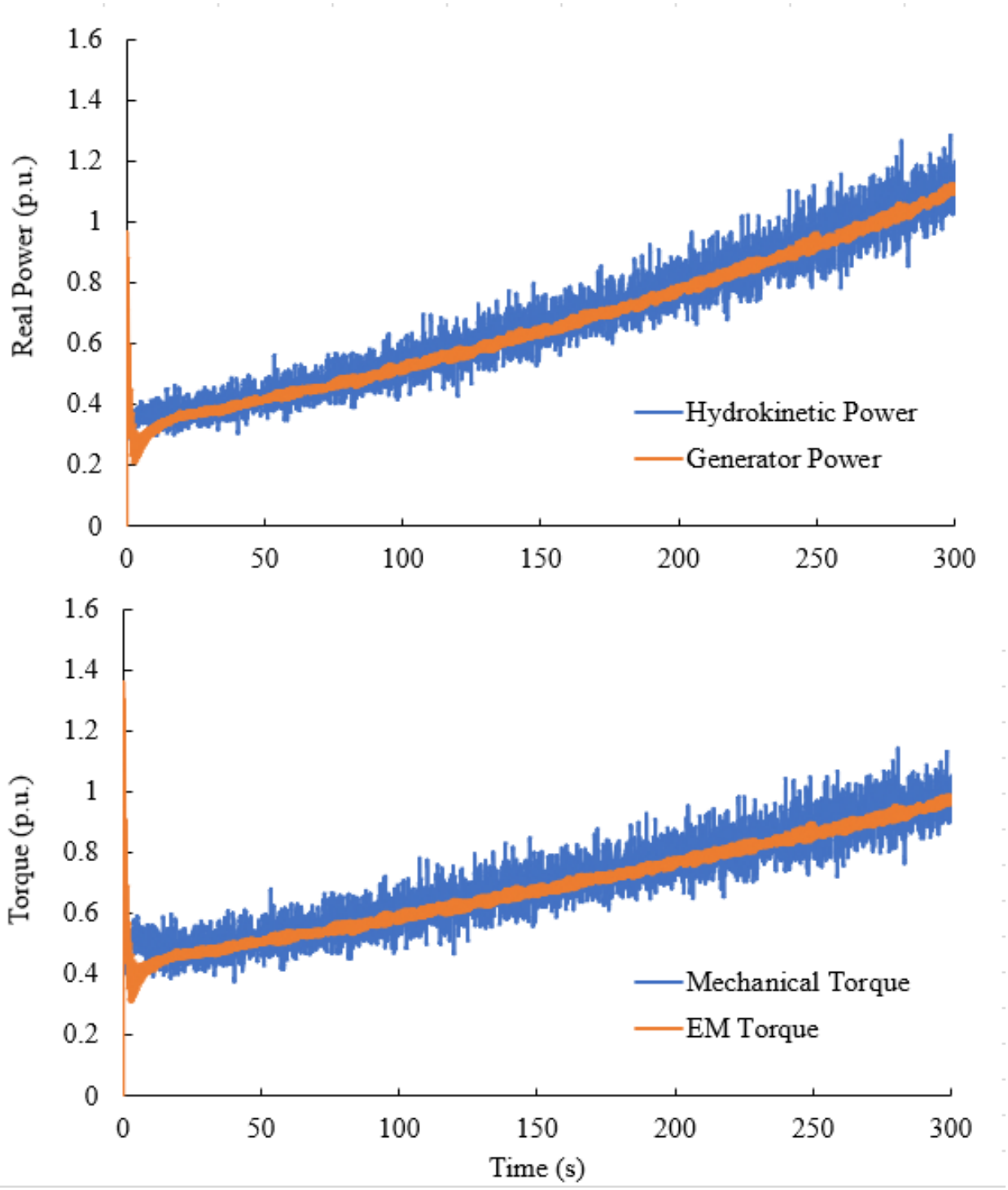

(b) Power and torque output of the PMSG and hydrokinetic turbine

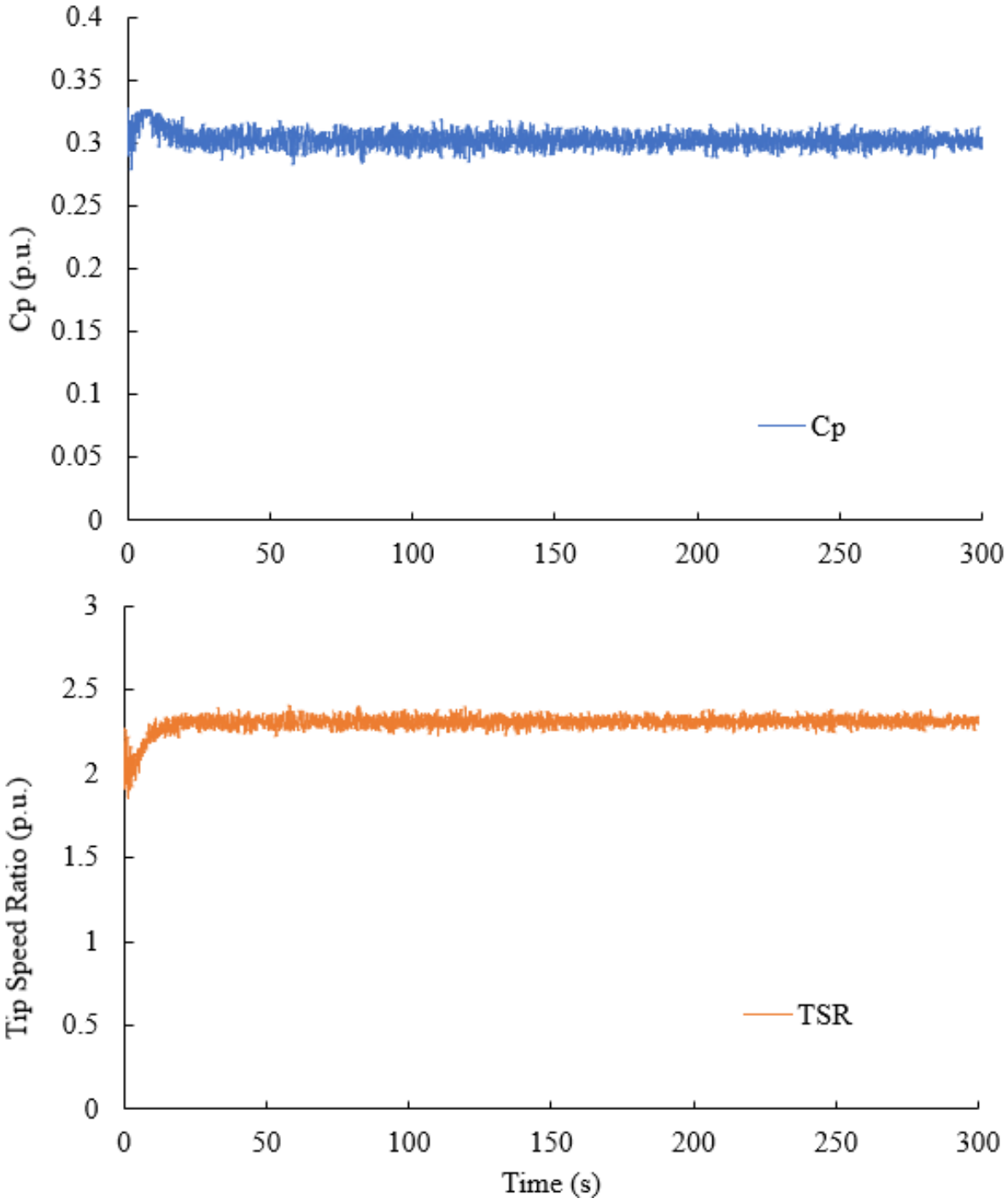

(c) Controlled Cp and TSR throughout the MPPT control

Figure 2.6. The outputs of the dynamic simulation for the machine side (PMSG and hydrokinetic turbine) with the MPPT.

2.4 Electrical Power Conversion and Power Converters

The outputs of the PMSG in the hydrokinetic power generation causes the variable frequency due to the variable rotational speed of the turbine that drives the PMSG. Hence, the power conversion process from the PMSG requires a set of power converters to transmit the stable power into the grid [2]. As shown in Figure 2.1, the first set of the power converters is the three-phase diode rectifier, called an "AC-DC" rectifier that converts the variable AC output of the PMSG into the DC voltage output. Because the hydrokinetic turbine directly drives the PMSG, the power output and operating speed are varied by the water flow. So, the AC-DC rectifier is required to convert this variable AC output into the DC output at the DC bus.

In the simulation of the complete model of the MHK power plant, the passive diode bridge rectifier shown in Figure 2.7 is used, and the output of the DC voltage throughout the diode rectifier is still proportional to the rotational speed. The following equation describes the output voltage from the per-phase equivalent circuit of the PMSG to the DC bus throughout the diode rectifier:

$$V_{dc} = \frac{3\sqrt{6}}{\pi} V_{ph} \tag{2.19}$$

$$V_{ph} = E_{ph} - j\omega_G L_s I_s \tag{2.20}$$

$$E_{ph} = k_\phi \omega_G \tag{2.21}$$

where V_{ph} is the per-phase voltage of the PMSG output, E_{ph} is the per-phase electromagnetic field of the PMSG, k_ϕ is the generator voltage constant, ω_G is the rotational speed of the PMSG in rad/s, L_s is the stator inductance, and I_s is the stator current toward the rectifier.

Then, the real power output of the PMSG can be expressed as:

$$P_{gen} = V_{dc} I_S = \frac{k_\phi^2 \omega_G \sin(2\delta)}{2L_s} \tag{2.22}$$

where δ is the power angle between E_{ph} and V_{dc}.

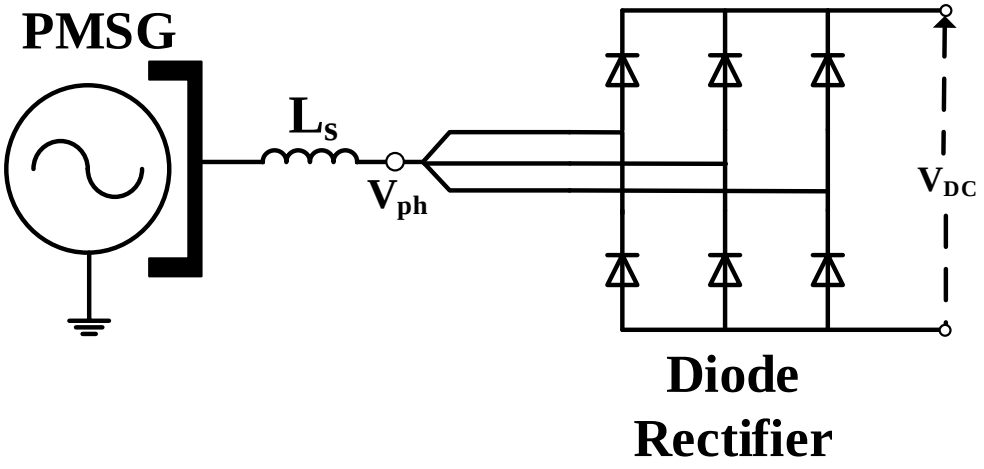

Figure 2.7. Equivalent circuit of the PMSG connected to a passive diode bridge.

Since the output from the diode rectifier is a variable DC voltage, the DC voltage and current at DC bus are required to be maintained to provide the maximum power from the PMSG to GSC. Therefore, the passive diode rectifier in the hydrokinetic power generation requires the DC-DC converter (DC-DC boost converter is used in the simulation) to control the real power output even though the rotational speed of the PMSG varies. So, the DC-DC boost converter controls the output power of the PMSG to be maintained following the MPPT control, as mentioned in Chapter 2.3. The circuit topology of the DC-DC boost converter and its control diagram are shown in Figure 2.8. According to Figure 2.8(b), the controlled pulse width modulation (PWM) varies its width to control the switch of the power electronics, and the MPPT output power reference compared with the measured real power out of the diode rectifier determines the duty ratio of the DC-DC converter throughout the PI controller. The duty ratio is compared to the triangular wave at the switching frequency (e.g., 1 kHz), so it produces the corresponding PWM to produce the maximum power based on the MPPT control as ω_G and V_{DC} change. Therefore, following the explained control scheme in Figure 2.8(b), the switch of the

DC-DC boost converter turns on and off to control the real power to be maximized. The duty ratio determines the switch's "on" time based on the real power reference as shown in Figure 2.8(b). In the digital simulation, no losses through the DC-DC boost are assumed, so the input power and output power out of the boost converter are considered to be equal.

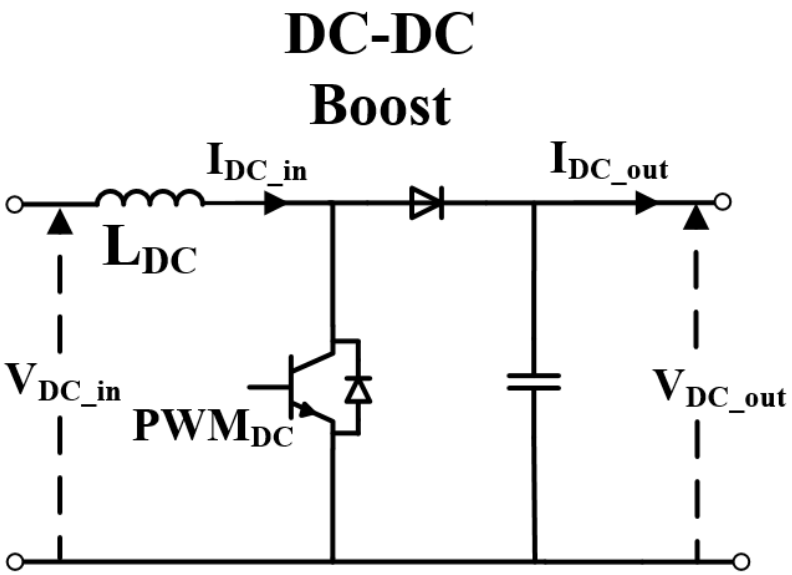

(a) Circuit diagram of the DC-DC boost converter

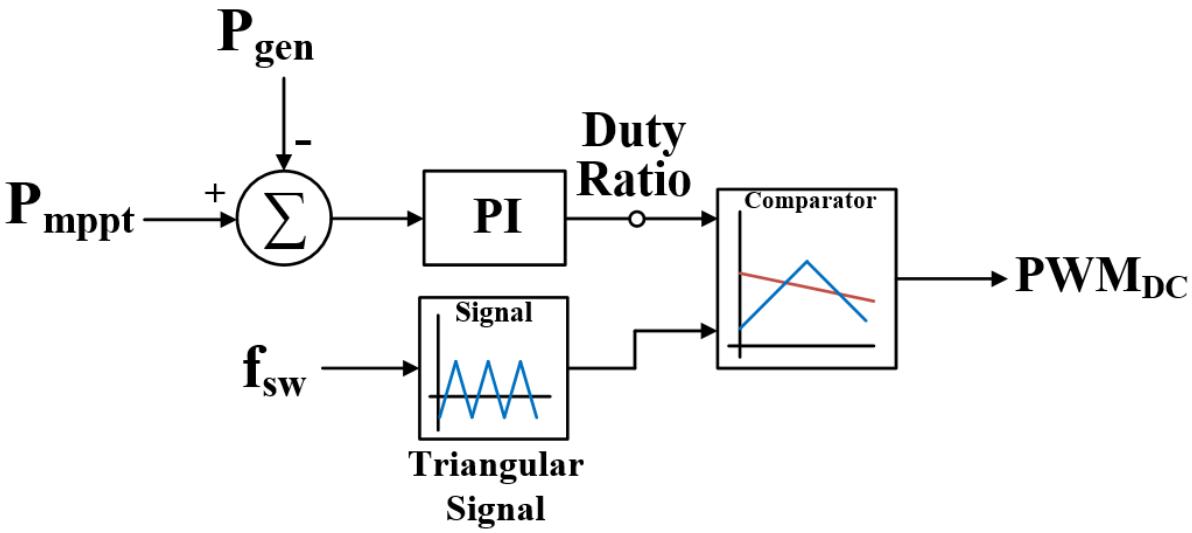

(b) The control scheme of the PWM for the DC-DC boost converter

Figure 2.8. Circuit topology and control scheme of the DC-DC boost converter.

Because the DC-DC converter maintains the real power output based on the MPPT, the real power output to the DC bus can be maintained at any rotational speed of the PMSG by controlling the duty ratio. Now, the AC-DC diode rectifier and the DC-DC boost converter are defined as “Machine Side Converter” (MSC) in this thesis. In the MSC, however, the control function that maintains the DC bus voltage constant does not exist; therefore, the DC-AC converter in the GSC is responsible for maintaining the DC voltage constant.

The DC-AC inverter, or the GSC, has responsibility to keep the DC bus voltage constant regardless of the magnitude of the fluctuating generator power, and it matches the DC bus voltage to the voltage ratings of the power switches in the DC-AC inverter. The DC-AC inverter also needs to control the active and reactive power flow between the grid and the GSC by adjusting the active and reactive currents. In the dynamic simulation of the complete converter model, the DC-AC inverter is made up of three-phase IGBTs, as shown in Figure 2.9, and they are operated as the current source inverter. The DC-AC inverter contains the q-axis and d-axis current controller; the current controller converts d-q currents to controlled three-phase currents for the DC-AC inverter throughout the inverse of Park Transformation as mentioned previously in the equation (2.3). The inverter tracks the phase angle of voltage at the grid (V_{grid}) and synchronizes it to the DC-AC power converter with the use of the phase-locked loop; hence, the changes in the phase angle and the frequency will be tracked because the DC-AC converter is locked to the phasor of the grid voltage [2]. Therefore, it controls the active and reactive power flow between the grid side and the machine side of the hydrokinetic power system, independently. Figure 2.10 demonstrates the control scheme of the DC-AC inverter as it is explained. The d-q currents on the GSC are controlled to maintain the DC bus voltage constant and keeps the AC voltage as constant as possible. Because the GSC manages the active and

reactive power flow to the grid side, it simulates the impact of the grid side characteristics on the power fluctuation. The GSC interacts with the grid status, so the dynamic simulation of the hydrokinetic power system can be influenced by the grid condition such as the short circuit ratio and impedance angle and analyze the voltage fluctuation at the grid. The q-axis current (reactive current) in the GSC will be replaced with other control techniques in the future chapter to mitigate flicker, focusing on the main objective in this thesis.

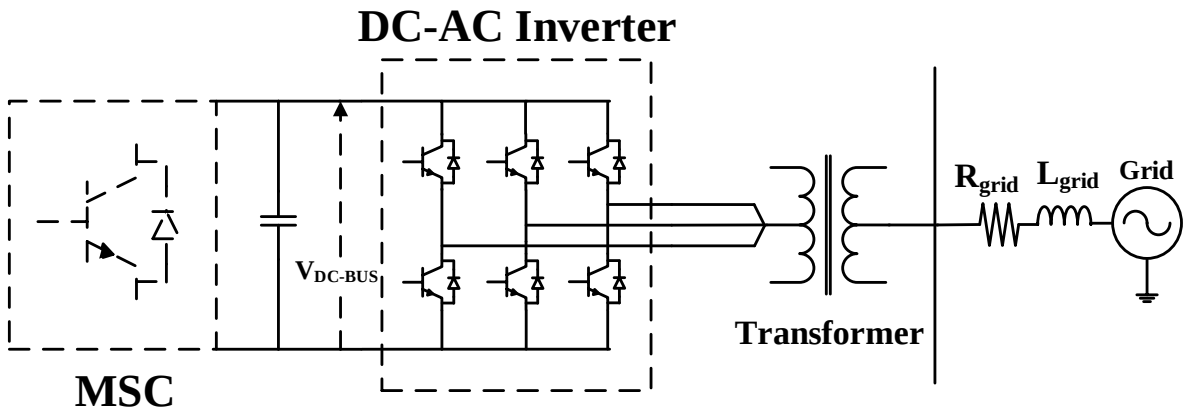

Figure 2.9. Circuit diagram of the DC-AC inverter connected to the grid

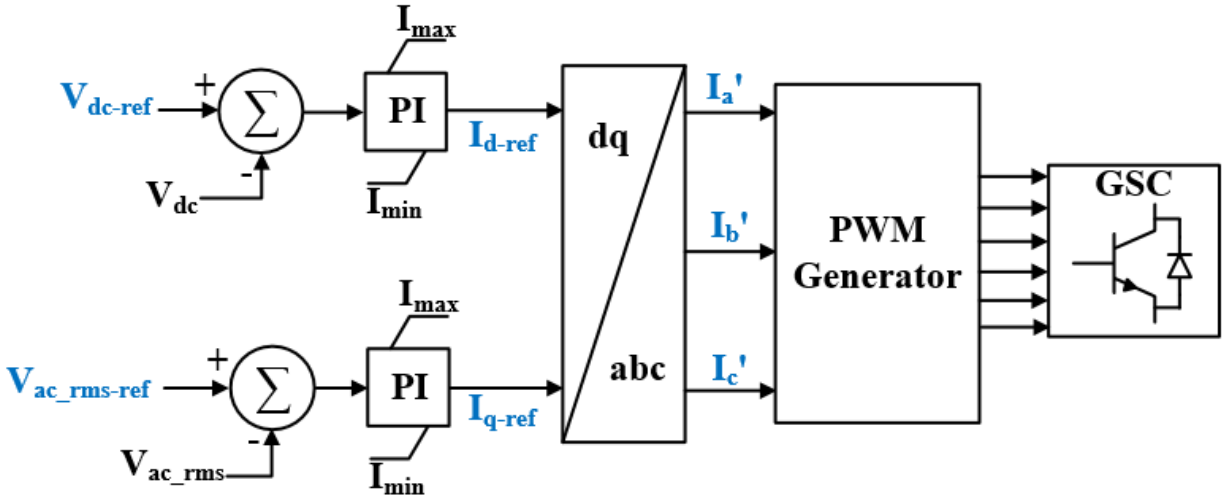

Figure 2.10. Control scheme of the DC-AC inverter using d-q current control

The above electrical power conversion model includes the detailed PWM converter model. For the detailed PWM voltage-source converter models on the MSC and GSC, the electrical components that are switched on and off at high switching frequency require small simulation time steps; therefore, the simulation of the complete model of power converters makes the simulation time slower [15]. However, the detailed model of the back-to-back converter with long simulation time is inappropriate in the case of flicker assessment because it requires at least 10 minutes of the simulation time. In the case study, therefore, the average model of the power converters without the PWM switches, as described in [28], [29], is used for the flicker assessment instead of the detailed model of the power converters. In the average model, the back-to-back converter with the PWM is replaced by the controlled dependent voltage sources. Figure 2.11 shows the simplified model of the MHK power generation used in the case study simulation that requires the flicker assessment. In the simplified model, the simulation starts with the DC circuit model without the MSC controller. In Figure 2.11, the DC circuit includes the DC capacitor and two dependent current sources. The input currents on each current source are determined by:

$$I_{dc\_in} = \frac{P_{gen}}{V_{dc}} \tag{2.24}$$

$$I_{dc\_out} = \frac{P_{ter}}{V_{dc}} \tag{2.25}$$

where P_{gen} is the reference real power output that is obtained from the machine side simulation (working independently), P_{ter} is the real power output at the terminal (grid side), and V_{dc} is the DC-bus voltage. Then, the DC bus voltage in the simplified converter model can be expressed as:

$$V_{dc} = \frac{1}{C}\int (I_{dc\_in} - I_{dc\_out})\, dt + V_{dc\_0} \tag{2.26}$$

where C is the capacitor value, and V_{dc_0} is the initial DC voltage. Therefore, without the MSC controller (AC-DC and DC-DC converter), the DC circuit on the machine side can deliver the corresponding currents determined by the maximum real power of the hydrokinetic turbine. Then, the DC-AC inverter is replaced by the controlled dependent voltage sources, and it is controlled by the desired voltage signals based on the control task of the GSC as described in Figure 2.10. Therefore, the simplified model improves simulation speed and independently controls the machine side and grid side of the MHK power generation. In the simplified model, no losses throughout the converters are assumed.

The description of the theoretical modeling of the MHK power generation and the process of the electrical power conversion for both complete model and average model of the MHK power generation in the digital simulation have been presented in this chapter. In the next chapter, the three different control schemes for flicker mitigation will be presented, using the theoretical model of the MHK power generation described in this chapter.

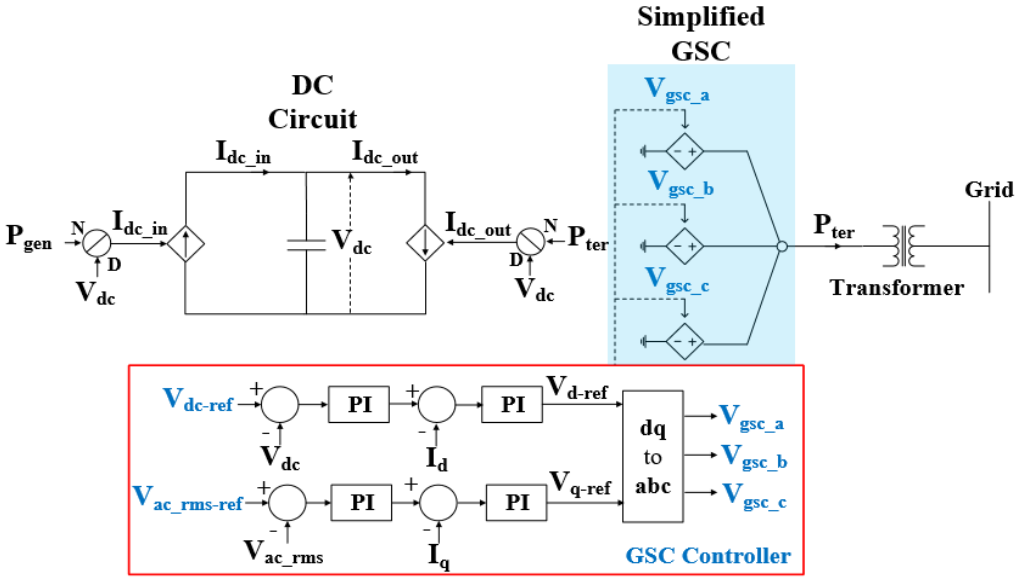

Figure 2.11. The simplified model of the MHK power generation used in the case study

3. Control Functions of MHK Power Generation for Flicker Mitigation

3.1 Function. 1: Reactive Power Compensation (VAR Control)

In the variable speed turbine with the back-to-back converter, the reactive power control can be implemented in the GSC so that the voltage source converter in the GSC compensates the reactive power behaving similarly to a STATCOM [30]. The reactive power compensation (VAR control) in the GSC regulates voltage fluctuation across a power line connected to the grid by using the reactive power to drop the voltage throughout the line impedance. Figure 3.1 shows the equivalent circuit of the power system connected to the grid and its phase diagram to compass the calculation of dropping voltages in terms of real and reactive power and the idea of the VAR control. The voltages and currents in the electrical network can be determined through complex notation. In the power flow system, active power (P) and reactive power (Q) on load buses are generally given, and often the resistance of lines is negligible compared with reactance.

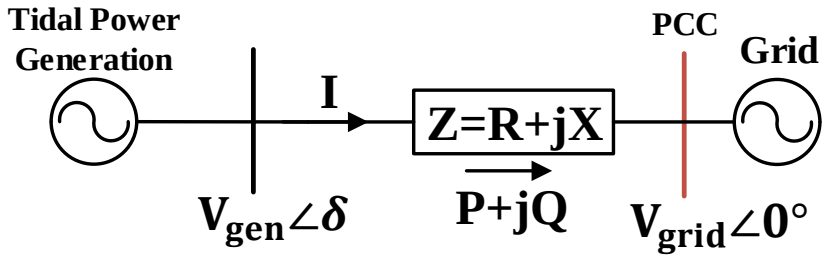

(a) The equivalent circuit for power system connected to the grid

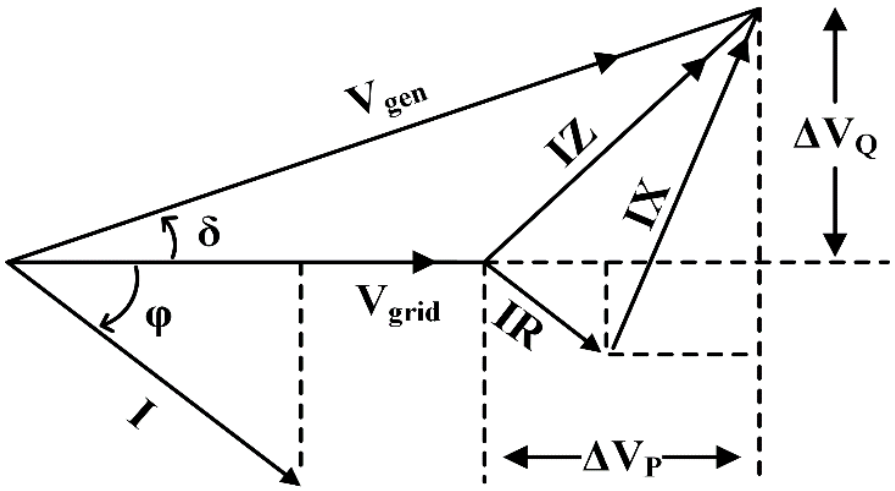

(b) Phase diagram of the equivalent power system.

Figure 3.1. Diagrams understanding Reactive Power Compensation

From Figure 3.1(a), the voltage drop across the power line will be given as:

$$\Delta V = V_{gen} - V_{grid} \tag{3.1}$$

where V_{gen} represents the voltage on the generator side, and V_{grid} represents the voltage on the grid side. The quadratic form of the voltage drop in reference to Figure 3.1(b) can be rewritten as:

$$\Delta V = \Delta V_P + j\,\Delta V_Q \tag{3.2}$$

$$V_{gen} = \left(V_{grid} + \Delta V_P\right) + j\,\Delta V_Q \tag{3.3}$$

Based on Figure 3.1(b) and equation (3.3), the voltage drop of each complex form can be expressed as:

$$\Delta V_P = \left(\frac{RP + XQ}{V_{grid}}\right) \tag{3.4}$$

$$\Delta V_Q = \left(\frac{XP - RQ}{V_{grid}}\right) \tag{3.5}$$

In the distribution network where the X/R ratio is small, angle δ is small, and ΔV_Q becomes almost zero. Therefore, the simulation maintains ΔV_Q to be zero to keep a unity power factor. Hence, the voltage drop is solely determined by ΔV_P following as:

$$\Delta V \cong \frac{(RP + XQ)}{V_{grid}} \tag{3.6}$$

From the equation (3.6), the voltage drop is dependent on the grid impedance (X_{grid} and R_{grid} in this dynamic simulation) and P and Q to the grid; therefore, both grid impedance and fluctuation in generator power will cause the voltage drop at the grid. In order to make the voltage drop zero, the reactive power on the grid side should be controlled as following this equation:

$$(RP + XQ) = 0$$

$$Q = -\left(\frac{RP}{X}\right) \tag{3.7}$$

Therefore, the VAR control implemented in the GSC regulates the reactive power following equation (3.7) to minimize the voltage drop at the grid. The VAR control is possible to minimize the voltage drop only if X and R of the grid and P are given. Therefore, the line impedance and the real power output need to be set as the reference values for the VAR control.

The control scheme of the GSC, including VAR control, is shown in Figure 3.2. The VAR control scheme in the GSC is similar to the basic control scheme of the DC-AC inverter in Figure 2.10. Instead, the VAR control sets the compensated reactive power as the reference values for the inner current control loop in q-axis. From the equation 3.7, the amount of the reactive power to mitigate flicker will not be enough if the reactance of the X is greater than its

R. For example, in the distribution network with a very low impedance angle where it has a very low X/R ratio, the VAR control will not be effective in mitigating voltage fluctuation, still causing flicker.

The operating capacity of the reactive power in the GSC is limited by the maximum current carrying capacity to prevent the damage of the IGBT, so the current limiter is usually implemented for the protection of the IGBTs in GSC [2]. As a result, there is an operating limit of the GSC that has a limited amount of the reactive power generated by the maximum current carrying capability of the IGBTs to mitigate the voltage fluctuation. The limitation of the VAR control implemented in the GSC for flicker mitigation is investigated by the case study and assessment of flicker severity level in particular when the X/R ratio is low.

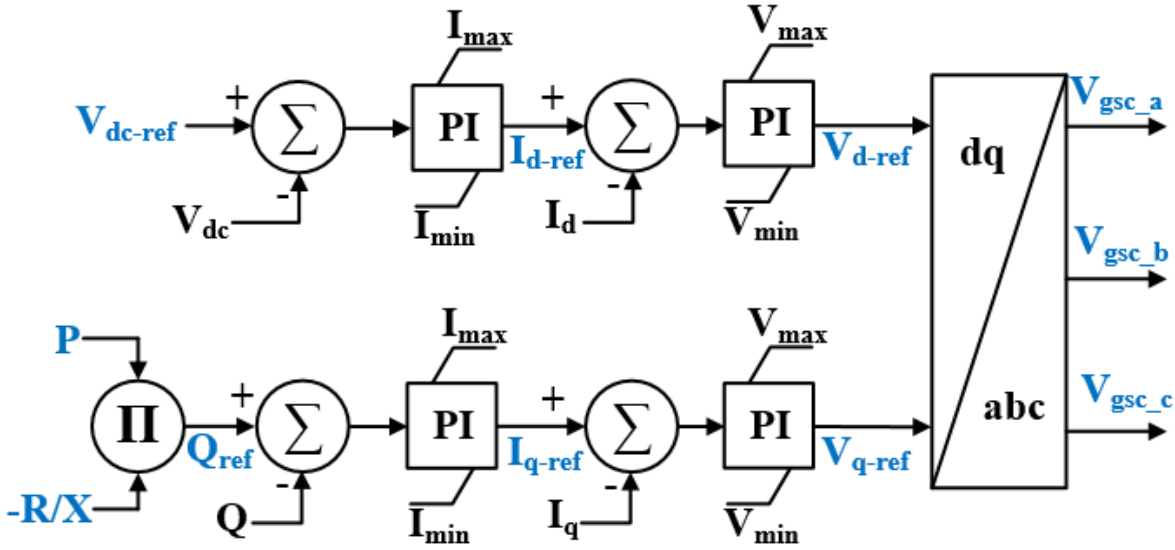

Figure 3.2. Control scheme of VAR control in GSC

3.2 Function. 2: Battery Energy Storage System (BESS) Control.

In this thesis, flicker mitigation within the distribution network where the X/R ratio is low shall be considered. This type of grid condition causes voltage fluctuations to be dominant to real power fluctuations. Besides, there is a limit to the amount of reactive power supplied by the GSC when the grid reactance is not much greater than the grid resistance [20]. Thus, the reactive power compensation alone is insufficient to mitigate flicker on the grid. Therefore, this thesis proposes the BESS as another solution to mitigate flicker of the MHK power plant. The BESS can effectively smooth the real power fluctuation and finally mitigate flicker even in the case of the low X/R ratio.

Instead of the BESS, implementation of a supercapacitor would effectively mitigate the power fluctuation of the renewable resources because a supercapacitor has faster discharging and charging time, a larger number of cycles and higher cycle efficiency than the BESS does; however, a supercapacitor is too excessive to be used in mitigation of voltage fluctuation of this type of application, and it is ten times more expensive than lithium-ion battery energy system [32]. Therefore, a supercapacitor is not financially viable and too excessive to be used in this study.

In the digital simulation, the BESS is controlled to charge and discharge the fluctuating real power due to water turbulence. Hence, the output power to the grid will have minimum turbulent content, and the voltage fluctuation on the grid will be minimized too. The battery model, the circuit topology of the BESS system, and the BESS control scheme for flicker mitigation are shown in Figure 3.3. The BESS is installed on the DC Bus of the MHK power generation, and it consists of two main parts: a lithium-ion battery and bidirectional DC-DC converter (configured as the buck converter in one power flow direction and configured as the

boost converter in the opposite power flow direction) as shown in Figure 3.3(b). In the PSCAD simulation, the lithium-ion battery pack is used with simplifying assumptions such as constant internal resistance and no temperature influence on the battery system. The specification of the lithium-ion battery pack used in the case study follows the basic characteristics of the battery used in the energy storage system, and it is commercially available [33], [34].

The battery model used in the simulation is the simplified Shepherd's battery model; the dynamic model of the battery consists of the controlled voltage source in series with an internal resistance [35], as shown in Figure 3.3(a). The internal voltage of the battery used in the simulation is defined as:

$$\mathrm{E_{batt}} = E_0 - K\frac{q}{q - it} + a \cdot e^{-b \cdot it} \tag{3.8}$$

where E_0, K, q, it, a, and b are battery constant voltage, polarization voltage, battery capacity, actual battery charge over time t, exponential zone amplitude, and exponential zone time constant inverse, respectively. The state of charge (SOC) that indicates the charge of the battery in percentage is calculated at each time step as:

$$\mathrm{SOC} = \frac{\mathrm{q} - \int i_{\mathrm{batt}} dt}{\mathrm{q}} \tag{3.9}$$

where $\mathrm{i_{batt}}$ is the current flow over the battery, as shown in Figure 3.3(a).

Therefore, the terminal voltage of the battery is defined as:

$$\mathrm{V_{batt}} = E_{batt} - R_{batt} \cdot i_{batt} \tag{3.10}$$

where R_{batt} is the internal resistance of the battery.

Then, the battery model, as shown in Figure 3.3(a), is connected to a bidirectional DC-DC converter with buck and boost converter, as shown in Figure 3.3(b). Each IGBT of the converters receives the controlled signal (i.e., S_{Buck} and S_{Boost}) from the BESS controller in Figure 3.3(c). The mitigated power delivers to the grid since the BESS is connected to the DC bus of the back-to-back converter of the MHK power generation.

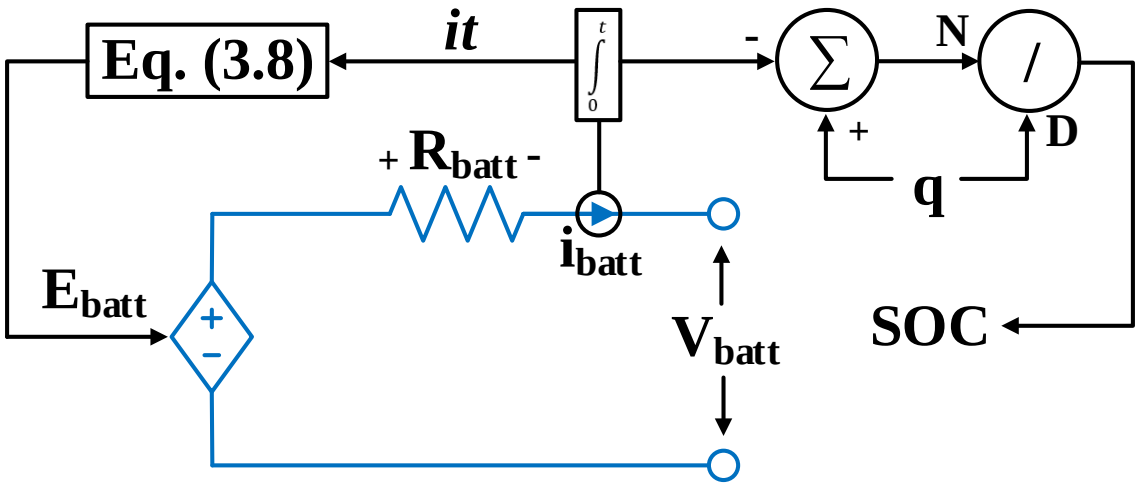

(a) Battery model.

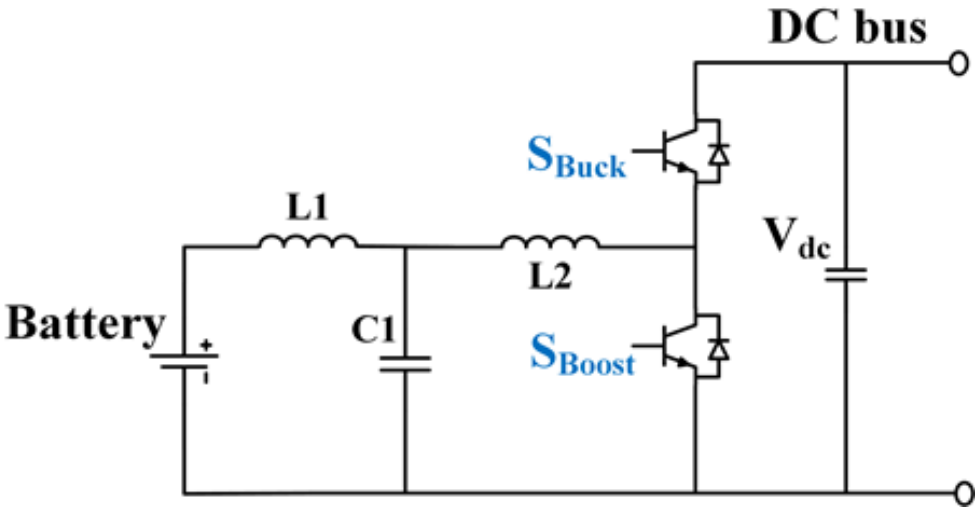

(b) Physical diagram of the BESS with the Converter

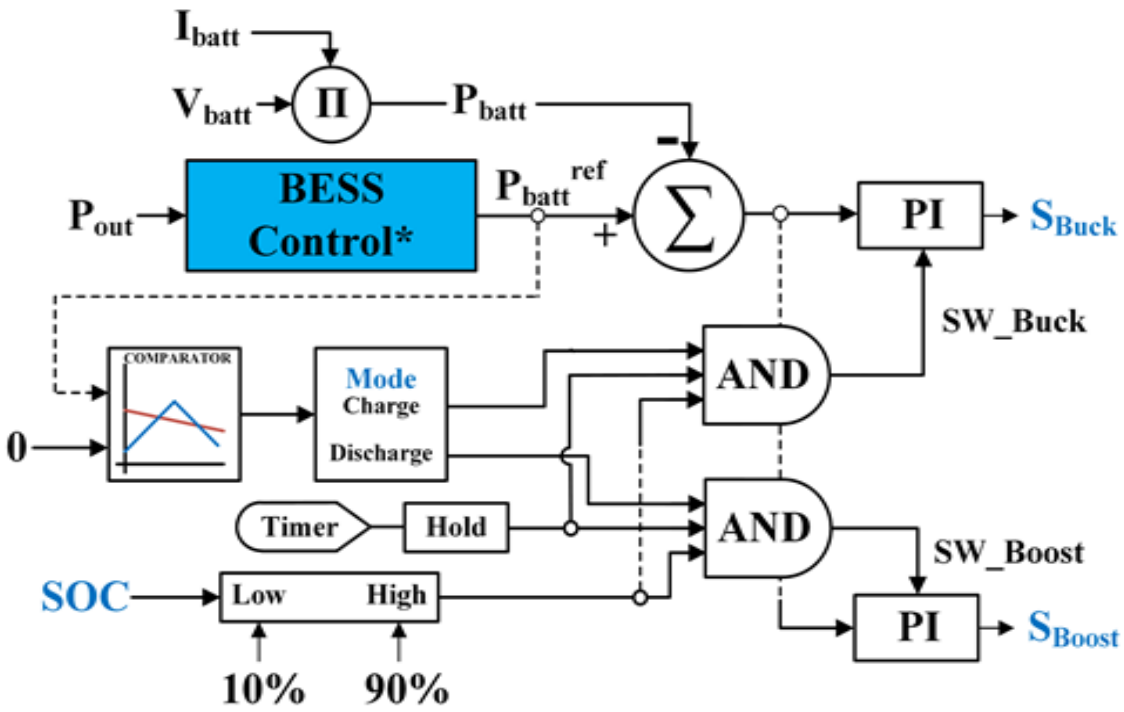

(c) The control scheme of the BESS

Figure 3.3. BESS dynamic simulation model and control scheme

As mentioned previously, there is a limit of flicker mitigation using only reactive power compensation under a certain type of grid condition. Instead, the BESS charges and discharges the fluctuating real power and smooths the power fluctuation and voltage flicker in the grid regardless of the grid conditions in the MHK power generation.

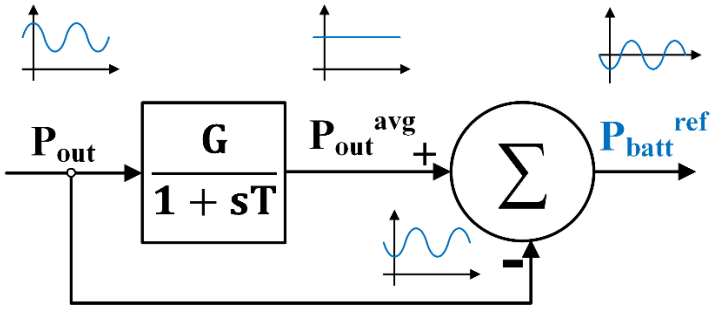

Figure 3.4. Block diagram of battery power reference for the BESS control

Figure 3.4 shows the process that determines the reference battery power output of the BESS for flicker mitigation. The reference power for the battery output (refer to P_{batt}^{ref} in Figure 3.3(c)) is determined by the fluctuating real power output of the MHK power system to the grid (P_{out}) subtracting the average power output (P_{out}^{avg}). Hence, based on the value of P_{batt}^{ref}, the decision of charging and discharging the battery is made by the buck and boost converters implemented in the BESS. For example, if P_{batt}^{ref} is less than zero, the buck converter is operated to charge the battery power; if P_{batt}^{ref} is greater than zero, the boost converter is driven to discharge the battery power. The amounts of charging and discharging battery power are determined by the amount of P_{batt}^{ref} through the PI controller of the converters. Therefore, the controlled BESS can deliver the smoothed power output from the MHK power generator to the grid, reduce the real power fluctuation, and finally mitigate flicker at the grid.

In the simulation, the BESS can be operated only if the SOC is between 10% and 90%. Therefore, the controller of the DC-DC converter allows each converter to be operated only if the SOC is within the range, as shown in Figure 3.3(c). In addition to the SOC requirement, the controller of the BESS requires a few seconds of delay to wait until the simulation system becomes stabilized. Then, based on the mode selection (charging or discharging), controlled PWM values (S_{Buck} and S_{Boost}) determine the amount of real power to be charged and discharged to mitigate the real power fluctuation. In Figure 3.3(b), each parameter and the specification of the DC-DC converter in PSCAD simulation are based on the model provided in the PSCAD library, which is commercially available.

The BESS control effectively charges and discharges the battery power for flicker mitigation regardless of the grid conditions. It also monitors the amount of input and output of the real power of the MHK power generation. However, the BESS may be exaggerated due to its

cost and the size of the MHK power generation; hence, the installation of the BESS to the hydrokinetic power system shall be hesitated based on the site where the tidal power plant is installed and the grid where the other applications would not sufficiently mitigate the voltage fluctuation. In order to overcome these disadvantages of the BESS, the $I_q - V_{grid}$ adaptive control, so-called adaptive control in this thesis, is suggested in the next subsection.

3.3 Function. 3: $I_q - V_{grid}$ Adaptive Control

The previous two controls for flicker mitigation (VAR compensation and BESS) have a few disadvantages on each. For example, the VAR control on the GSC might not sufficiently mitigate flicker when the control gain for the VAR control is not rapid enough to respond to the severe and fast changes in the voltage fluctuation in the case of the low X/R ratio of the grid condition and strong water turbulence. In addition, the control gains on the PI controller of the VAR control cannot be flexibly changed based on the severity of voltage flicker and grid conditions, so the control scheme cannot promptly respond to the voltage drops. In the BESS control, the most concerning problem is the cost of the BESS even though the cost of the BESS deployment becomes lower recently; however, based on the budget provided in the project and the grid condition where the other reactive power controls are not sufficient to mitigate flicker, implementation of the BESS into the hydrokinetic power plant still shall be considered.

In order to overcome the disadvantages of these two controls, this thesis proposes the adaptive control by injecting the different reactive powers with the $I_q - V_{grid}$ control scheme implemented in the GSC. The $I_q - V_{grid}$ characteristics are determined by the I_q (reactive current) capability of the GSC and the voltage setpoints of the tidal power plant (grid side voltage margin) that allow only the limited amount of the voltage fluctuation on the grid. The amount of injecting reactive power to the grid is flexibly determined by the gain of the $I_q - V_{grid}$

characteristics [36]. As mentioned earlier, the compensating reactive power into the grid can reduce the voltage fluctuation; the adaptive $I_q - V_{grid}$ control scheme determines the amount of injecting reactive power, and it can rapidly respond to the voltage fluctuation on the grid because the control gain (K_{QG}) of the $I_q - V_{grid}$ control (on the inner current control loop of the GSC) can be changed flexibly based on the severity of the voltage flicker and the available I_q to inject the reactive power to the grid.

I_q capability of the GSC can be determined by the rated current of the GSC and the active current out of the GSC [36], and its equation can be written as:

$$I_{qmax} = \sqrt{I_{Limit}^2 - I_d^2} \tag{3.11}$$

where I_{Limit} is the rated current of the GSC, and I_d is the active current out of the GSC. The diagram for the $I_q - I_d$ capability of the GSC is shown in Figure 3.5 as it is obtained in the equation (3.11).

As shown in Figure 3.5, the GSC operating at the low level of the active current I_d can compensate the high level of I_q, and degrading the active current I_d delivered to the GSC helps to inject more reactive power with the increased I_q in the case of the severe disturbance such as severe water turbulence or very weak grid condition. Therefore, the shifting operating points of I_q and I_d will affect the control gain (K_{QG}) of the adaptive control scheme, and responses for mitigating flicker based on flicker severity. Then, the $I_q - V_{grid}$ characteristics determines the control gain, and its characteristic curve is shown in Figure 3.6. As shown in Figure 3.6, when the voltage flicker becomes severe in case of the strong disturbance, the reactive current I_q should be increased to inject more reactive powers to mitigate the voltage fluctuation as the active current I_d is degraded as shown in Figures 3.5 and 3.6; therefore, the slope of the $I_q - V_{grid}$

characteristics curve becomes steeper, and it can be interpreted as the control gain of the $I_q - V_{grid}$ control, K_{QG}, becomes larger to mitigate flicker with faster response.

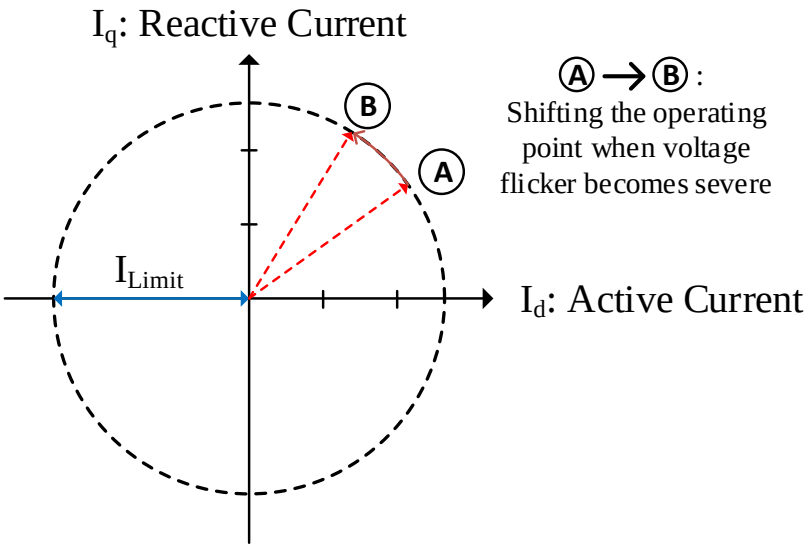

Figure 3.5. $I_q - I_d$ capability of the GSC

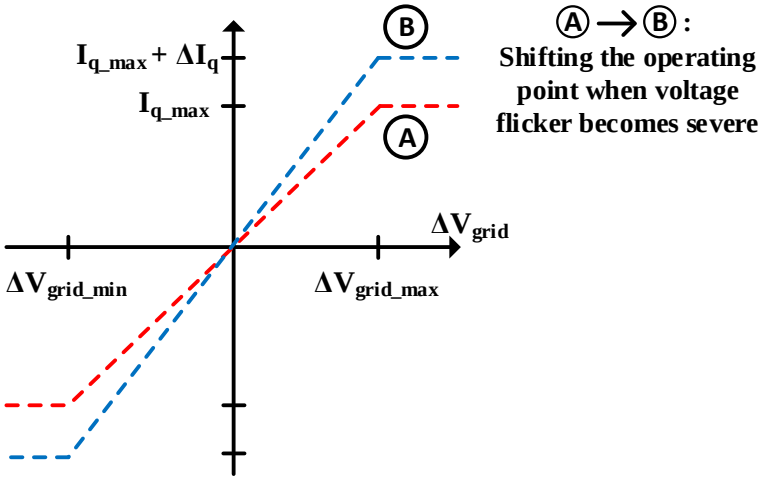

Figure 3.6. $I_q - V_{grid}$ characteristics curve

Now, the grid voltage set points shall be determined to limit the amount of the fluctuation of the voltage on the grid. In the simulation, the voltage fluctuation error can be tolerated up to $\pm$ 2.5% during the voltage flicker occurs, and the grid voltage reference is set to maintain in 1.0

per unit. Therefore, the difference of the maximum and minimum voltage set points ($\Delta V_{grid\_max}\ and\ \Delta V_{grid\_min}$) is set to 0.05 in the simulation so that it can tolerate voltage fluctuations up to $\pm$ 2.5%. The maximum and minimum I_q capabilities for GSC are assumed to have the same absolute value on each ($|Iq_{max}| = |Iq_{min}|$).

Then, the control gain for the I_q – $V_{grid,}$ which is K_{QG} is calculated as:

$$K_{QG} = \frac{I_{qmax} - I_{qmin}}{\Delta V_{grid\_max} - \Delta V_{grid\_min}} \tag{3.12}$$

To sum up the above equations and control logic for the I_q – V_{grid} adaptive control, the control scheme diagram for the I_q – V_{grid} adaptive control on the GSC is shown in Figure 3.7

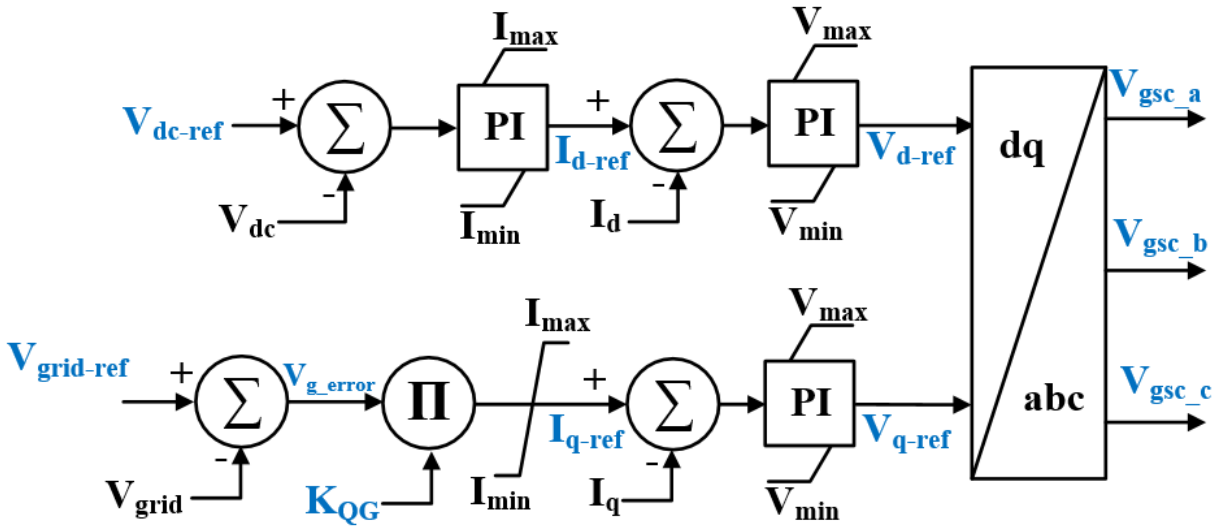

Figure 3.7. I_q – V_{grid} adaptive control in the GSC

4. Verification of the Proposed Control Functions through Digital Simulation

4.1. Simulation Background (Test System Overview and Case Scenarios)

Voltage fluctuation, or flicker, of the grid-connected MHK power generation, is induced by the water turbulence and grid conditions, as mentioned previously. In the case study, the default water flow characteristic is set to 3.2% of water turbulence intensity with 2.5 m/s of average water speed. However, the severity of the water turbulence will be varied based on the case scenarios. The specification of the MHK power generation in the PSCAD simulation model is shown in Table 1.

Table 1. Specification of the PSCAD simulation model

Tidal Power Generator	
Rated power of the turbine	1.0 MW
Rated power of the PMSG	1.2 MVA
Rated voltage of the generator	0.69 kV
Magnetic strength	1.0 p.u.
Stator winding resistance	0.017 p.u.
Stator leakage reactance	0.064 p.u.
Moment of inertia	0.7267 s
Mechanical damping	0.08 p.u.
Rated frequency	30 Hz
DC link voltage	1.5 kV
BESS	
Rated voltage of the battery	1.5 kV
Rated capacity of the battery	0.30 kA·hr
Rated voltage of the converter	1.7 kV
SOC range	10%-90%

To differentiate the grid condition of the grid-connected tidal power generation, a short circuit capacity ratio (SCR) and a grid impedance angle (φ) are changed as the variable factors of flicker emission in the case study. The two variable factors in determining the grid condition in this study case are SCR and X/R ratio φ, and they are defined as:

$$\mathrm{SCR} = \frac{S_k}{S_n} \tag{4.1}$$

$$\varphi = \arctan\left(\frac{X_{grid}}{R_{grid}}\right) \tag{4.2}$$

where $S_k$is the short circuit apparent power of the grid-connected to the turbine, or the grid fault level, S_n is the rated apparent power of the turbines, which is 1 MW. R_{grid} and X_{grid} are the resistance and reactance of the grid power line and represent the value of X and R in the equation (3.7). Therefore, SCR and φ are determined by the values of L_{grid} and R_{grid}, and the values of L_{grid} and R_{grid} are calculated as:

$$|Z| = \frac{U_r^2}{S_k} \tag{4.3}$$

$$R_{grid} = \frac{|Z|}{\sqrt{1+\varphi^2}} \tag{4.4}$$

$$L_{grid} = \mathrm{R} \cdot \varphi \cdot 2\pi f \tag{4.5}$$

where U_r is the rated line voltage on the grid, which is 20 kV, $|Z|$ is the magnitude of the impedance of the grid power line, and f is the frequency of the grid system, which is 60Hz. Therefore, the values of L_{grid} and R_{grid} determine SCR that represents grid stiffness and the X/R ratio that represents grid impedance angles or types of the distribution system. Hence, the simulation in this study can qualify the effectiveness of each control scheme on flicker mitigation

in different grid conditions determined by different values of L_{grid} and R_{grid}, or in varied water turbulence in each different case study.

The voltage fluctuation in the graph cannot objectively assess flicker severity; in order to accurately and objectively compare the efficiency of each control scheme for flicker mitigation, the quantification of flicker, or voltage fluctuation at the grid is essential. Therefore, the short-term flicker severity P_{st} that quantifies flicker level is calculated by flickermeter that is provided in MATLAB software, following IEC standard IEC 61000-4-15 [11] as mentioned in chapter 1.3. According to the IEC standard, flickermeter requires at least ten minutes (600 seconds) to measure P_{st}, which is defined as an integrated flicker over time and the percentile probability that a voltage fluctuation limit has been exceeded [11], [37]. The collected data of the grid voltage from PSCAD simulation are transferred into the input voltages of flickermeter in MATLAB, and P_{st} is calculated throughout the flickermeter model. The detailed flickermeter model and its process are already explained in chapter 1.3.

The PSCAD simulations use simulation time steps of 50 μsec and plot the outputs in every 10 msec. Since the digital flickermeter in MATLAB (built-in model) requires at least 60000 plots of time steps and rms grid voltages running for 600 seconds of the simulation time, the PSCAD saves 60000 data points of rms grid voltages with the above simulation time steps and transfers the grid voltage data into MATLAB workspace for the flickermeter to calculate P_{st} for each mitigation strategy.

To sum up the configuration of each control scheme for flicker mitigation in the simulation of the hydrokinetic power generation connected to the grid, Figure 4.1 demonstrates the arrangement of each control scheme in the tidal power generation and the assigned number of each scheme (VAR control, BESS control, and adaptive $I_q - V_{grid}$ control). Each control scheme

does not work together so that it will analyze the effectiveness of each control scheme on flicker mitigation, independently.

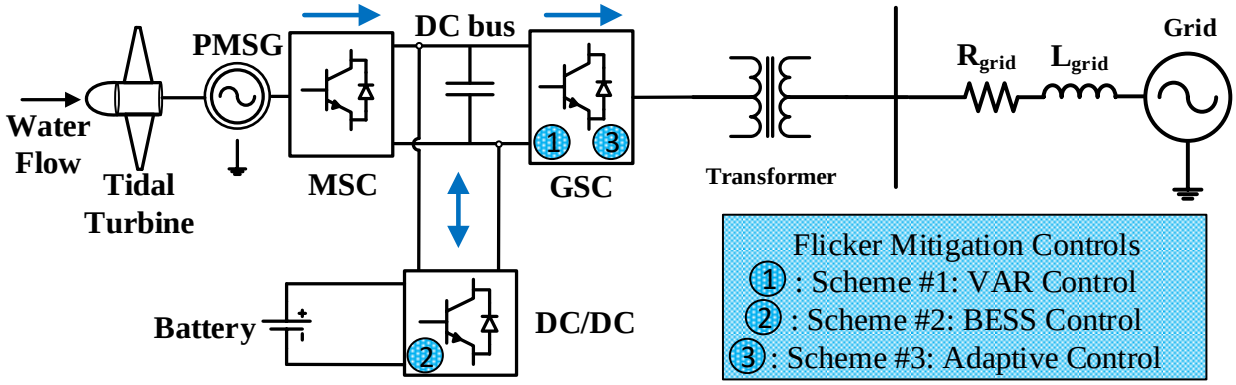

Figure 4.1. Configuration of the MHK power generation with each control scheme for flicker mitigation

4.2 Case 1: Varied SCR and X/R Ratio with Fixed Water Turbulence

In this study case scenario, the only grid condition determined by the SCR and X/R ratio is varied, while the water turbulence is constant as 3.2% of the turbulence intensity. SCR represents the stiffness of the grid that interprets the ability of the bus to maintain its voltage in response to the disturbance (stability of the grid voltage). At the power and voltage level used in the simulation, a system having "low" SCR value (i.e., $4 \leq SCR \leq 10$) that represents “weak” grid will experience more changes in the voltage fluctuation rather than "high" SCR (SCR > 20) that represents “stiff” grid in this thesis [38]. So, the "stiffness" of the grid is defined by SCR values in this simulation case study. X/R ratio is the ratio of the grid system reactance to the grid system resistance, stating the power factor of the system (the impedance angle of the grid). Usually, in the transmission line system, the X/R ratio could be high (i.e., 15 ~ 20 in this simulation). In the distribution network, the X/R ratio can be low (i.e., 1 ~ 5 in the simulation). X/R ratio affects the level of the short circuit current as of the following equation (4.3), and it

also influences the voltage deviation response to the active power or reactive power injection. For example, in the low X/R ratio, the voltage fluctuation is dominantly affected by the resistive component or the real power fluctuation, so the reactive power compensation will not be effective to mitigate the voltage flicker. Therefore, based on the X/R ratio, the implementation of the control scheme for flicker mitigation should be considered.

Figure 4.2 shows the results of the grid voltage, real power output, and reactive power output of each control scheme in the short-term view; the simulation in Figure 4.2 sets the grid status as the weak grid (SCR = 6) as the "worst" case within the distribution network that has X/R ratio of 1.025. Figure 4.3 demonstrates the results of the grid voltage, real power output, and reactive power output of each control scheme in the short-term view with the stiff grid (SCR = 25) with the X/R ratio of 15, and it represents the results in the grid condition that is stiff (not easily disturbed) with the relatively high X/R ratio.

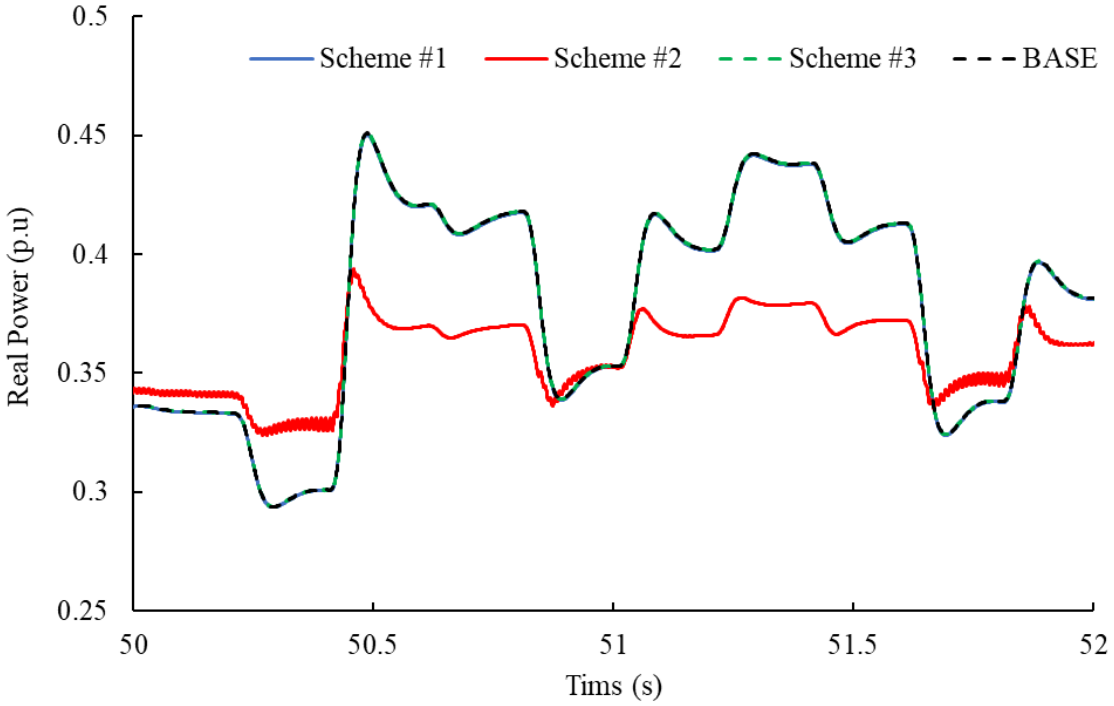

(a) Real power outputs from each control scheme

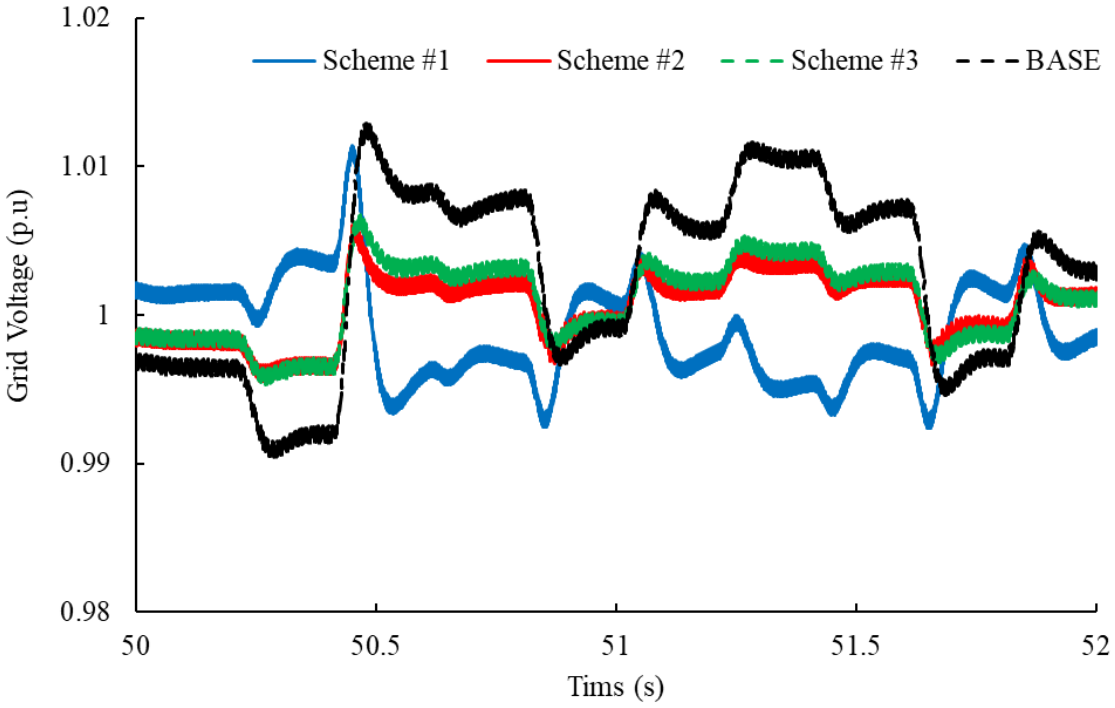

(b) Grid voltage outputs from each control scheme

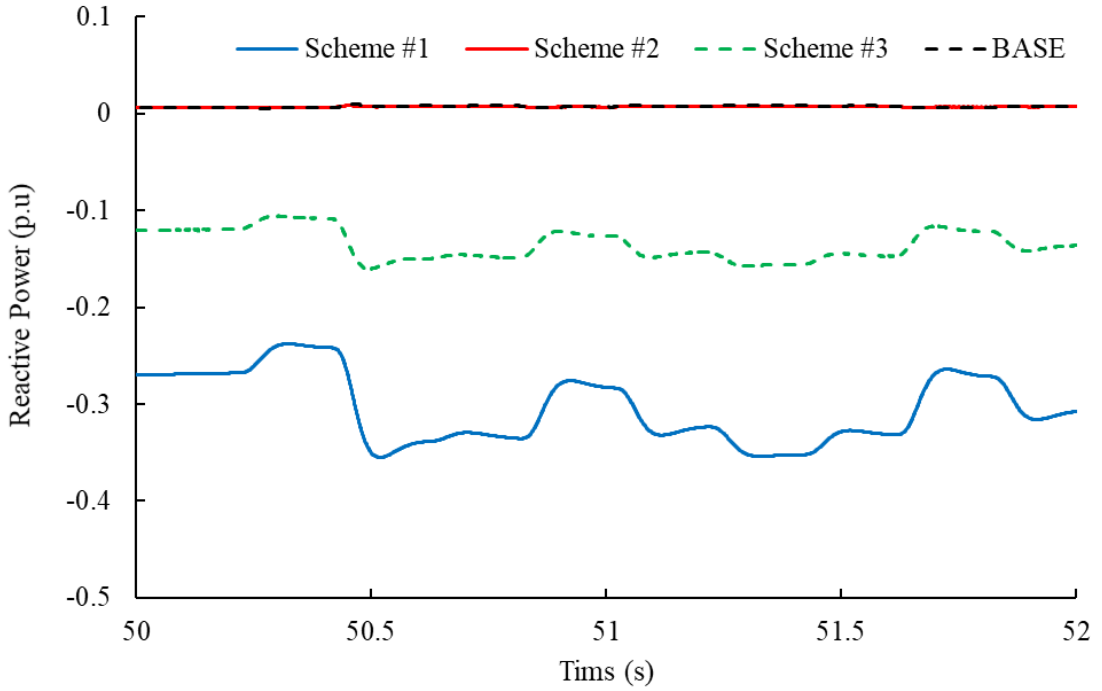

(c) Reactive power outputs from each control scheme

Figure 4.2. Simulation results for each control scheme when SCR = 6 and X/R ratio = 1.025

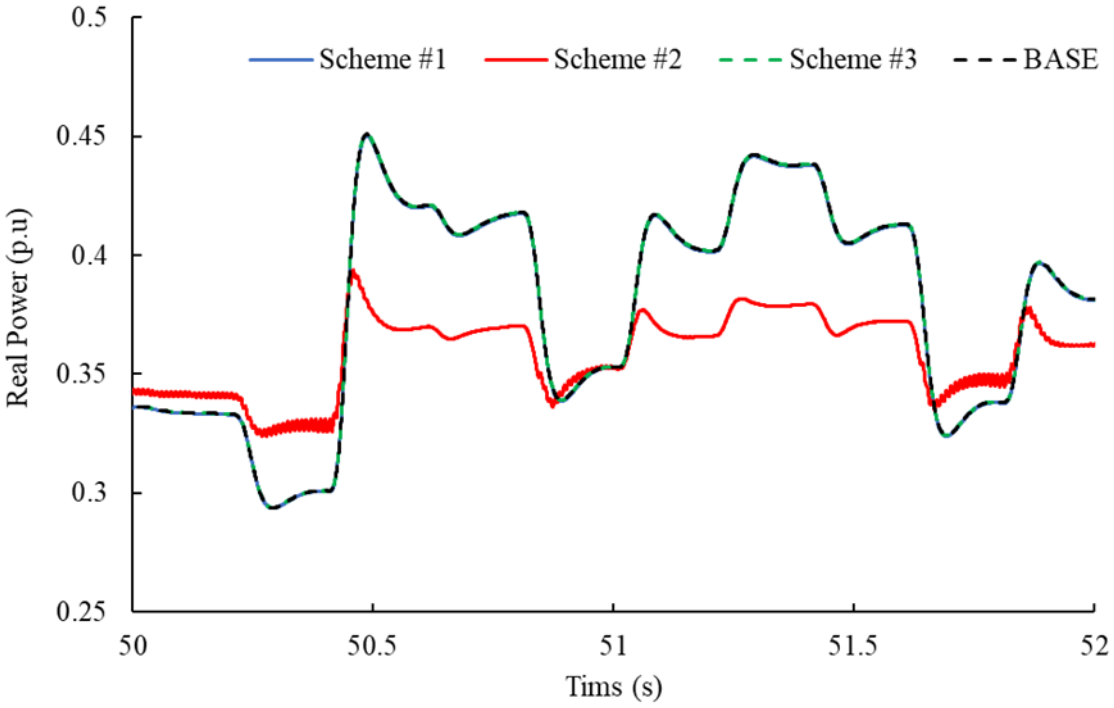

(a) Real power outputs from each control scheme

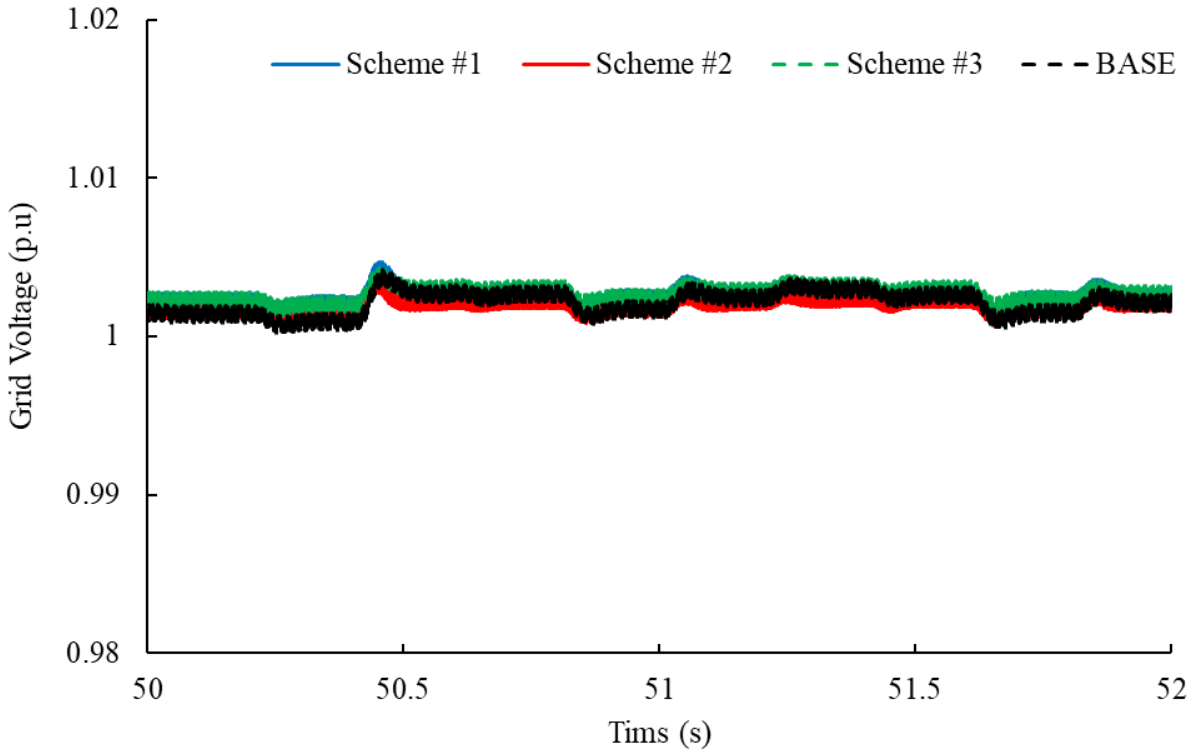

(b) Grid voltage outputs from each control scheme

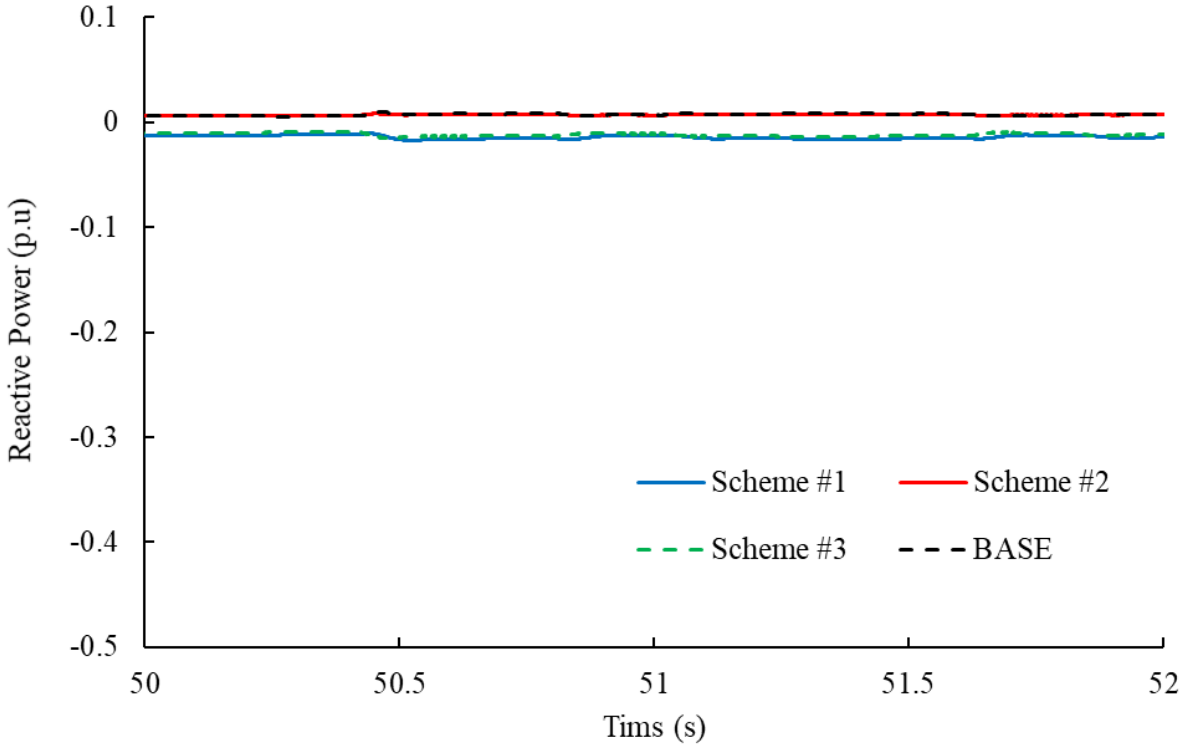

(c) Reactive power outputs from each control scheme

Figure 4.3. Simulation results for each control scheme when SCR = 25 and X/R ratio = 15

In both Figures 4.2 and 4.3, the black dash line, solid blue line, solid red line, and green dash line represent the base control without any mitigation techniques, VAR control, BESS control, and adaptive control, respectively. In Figure 4.2, the hydrokinetic power plant with the weak grid condition within the low X/R ratio network is manipulated, and the grid voltage shows very severe voltage flicker in the short-term view; however, in Figure 4.3, the grid condition is stiff with the high X/R ratio, so the grid voltage is not easily disturbed by the real power fluctuation caused by the water turbulence unlike Figure 4.2. Both real power outputs in Figures 4.2 and 4.3 are affected by the same water turbulence intensity; the grid voltage outputs in two different grid conditions indicate that the weak grid and low X/R ratio induce more severe voltage flicker. According to the results in Figure 4.2(b), the VAR control seems not so much effective to mitigate flicker by comparison with the base control (i.e., no flicker mitigation

control); therefore, the reactive power compensation is very limited to mitigate flicker in the weak grid with the low X/R ratio.

As mentioned earlier, it is difficult to assess flicker severity by the graphs objectively. Hence, the quantification of flicker in the short-term, P_{st} is measured in each different grid condition to objectively compare the efficiency of each control scheme for flicker mitigation. Table 2 shows P_{st} of each control scheme within the stiff grid (SCR = 25) with the three different X/R ratios (X/R ratios = 15, 2, 1.025). Table 3 demonstrates P_{st} of each control scheme within the weak grid (SCR = 6) with the three different X/R ratios (X/R ratios = 15, 2, and 1.025).

According to Tables 2 and 3, the values of the P_{st} increase as SCR and X/R ratio of the grid decrease; it can verify that flicker in the power grid of the tidal power plant becomes severe when the SCR and X/R ratio is small. The standard IEC 61000-3-7 specifies observation intervals for flicker and the "compatibility level" for P_{st} as 1.0 for 10 minutes, and P_{st} that is greater than 1 indicates a relatively high perceptible probability of a flicker problem [39]. This case study assumes this compatibility level as a voltage quality reference point even though the compatibility levels for MV or HV systems are not specifically defined by IEC standards [39].

Therefore, in the weak grid with the low X/R ratio (low impedance angle of the grid), the VAR control has a limit to mitigate flicker. Still, the VAR control can moderately mitigate flicker when the X/R ratio is large regardless of the SCR. With the BESS and adaptive $I_q - V$ control, flicker is effectively mitigated even when the X/R ratio is small. The BESS control is the most effective way to mitigate flicker among the control schemes regardless of the SCR and X/R ratio, but it is least cost-effective and might need extra space for deployment of the BESS system. The adaptive control can also effectively mitigate flicker in every grid situation; however, the rated current of the IGBTs on the GSC should be large enough to inject a large

amount of the reactive current I_q when flicker is very severe with the poor grid condition. So, it also indicates that the size of the IGBTs and its corresponding costs for the power inverters should be considered too. Therefore, the control schemes should be determined by the grid status and cost. Figure 4.4 demonstrates the bar graphs for the summary of the results in Table 2 and Table 3.

Table 2. P_{st} in the stiff grid

SCR = 25 (Stiff grid)			
Control	P_{st} (X/R=15)	P_{st} (X/R=2)	P_{st} (X/R=1.025)
Base	0.1763	0.2461	**0.2926**
VAR	0.1675	0.2312	**0.2738**
BESS	0.1523	0.1817	**0.1891**
Adaptive	0.1541	0.2071	**0.2074**

Table 3. P_{st} in the weak grid

SCR = 6 (Weak grid)			
Control	P_{st} (X/R=15)	P_{st} (X/R=2)	P_{st} (X/R=1.025)
Base	0.3981	0.6027	**1.0610**
VAR	0.3292	0.4572	**0.9754**
BESS	0.2671	0.3576	**0.4435**
Adaptive	0.2883	0.3968	**0.5201**

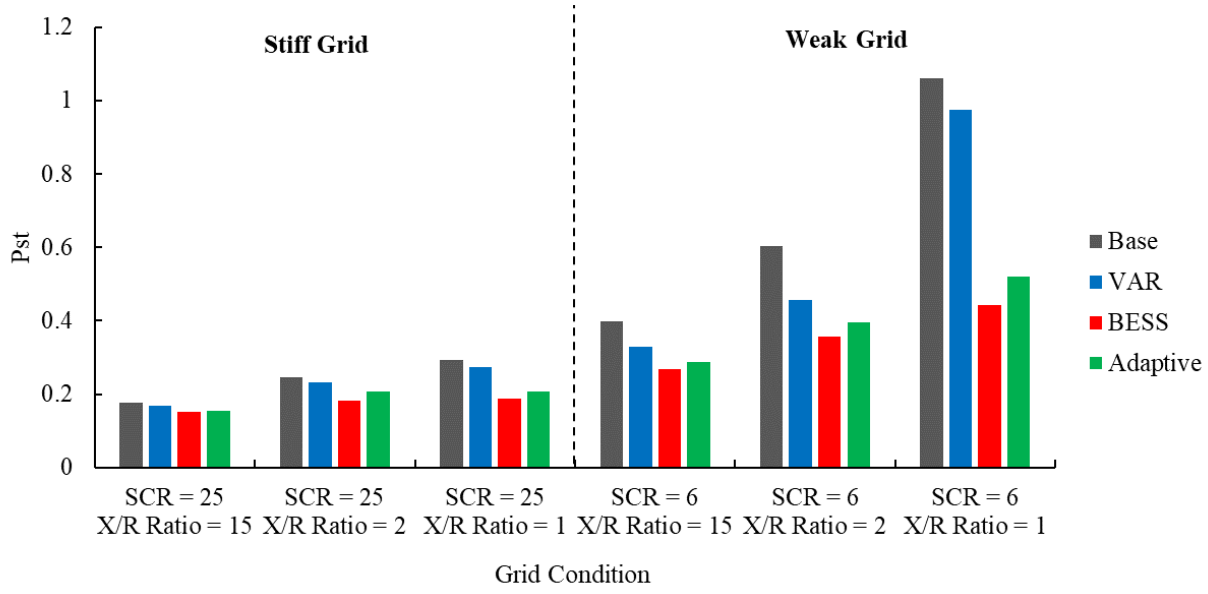

Figure 4.4. Summary of the results in case 1

4.3. Case 2: Varied Water Turbulence with Fixed SCR and X/R Ratio.

In this case scenario, the water turbulence is varied by changing the turbulence intensity %TI, but the SCR and X/R ratio which determines the grid condition are fixed to test the effectiveness of each flicker mitigation technique when the real power fluctuation caused by the water turbulence in the hydrokinetic power generation becomes greater or smaller. In order to assess P_{st} with the varied water turbulence in each different control scheme, the SCR is set to 6, and the X/R ratio is fixed to 2, so the differentiated values of P_{st} can be observed based on the different water turbulence.

Figures 4.5 and 4.6 demonstrate the water speeds, real power outputs of the MHK power generation, and the voltage at the grid with the water turbulence 7.2% and 11.6% for each control scheme. Compared with the real power fluctuation in Figures 4.2 and 4.3, the real power fluctuation and grid voltage fluctuation becomes more severe in Figures 4.5 and 4.6.

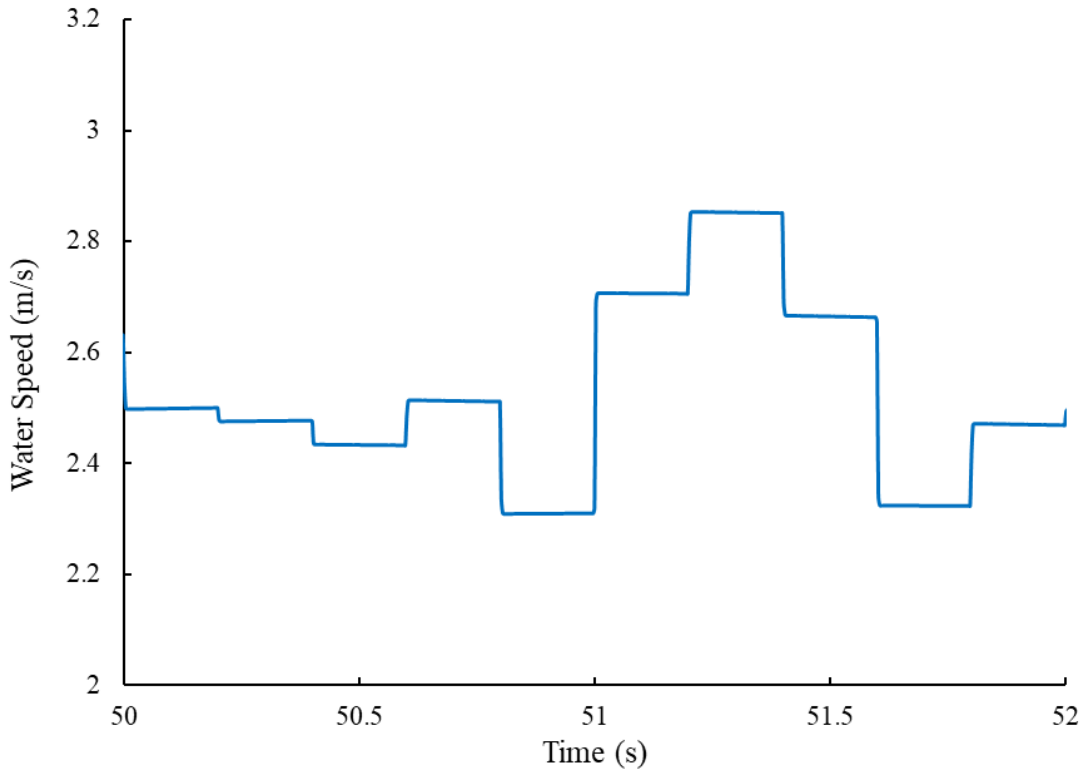

(a) Water speed with %TI = 7.2%

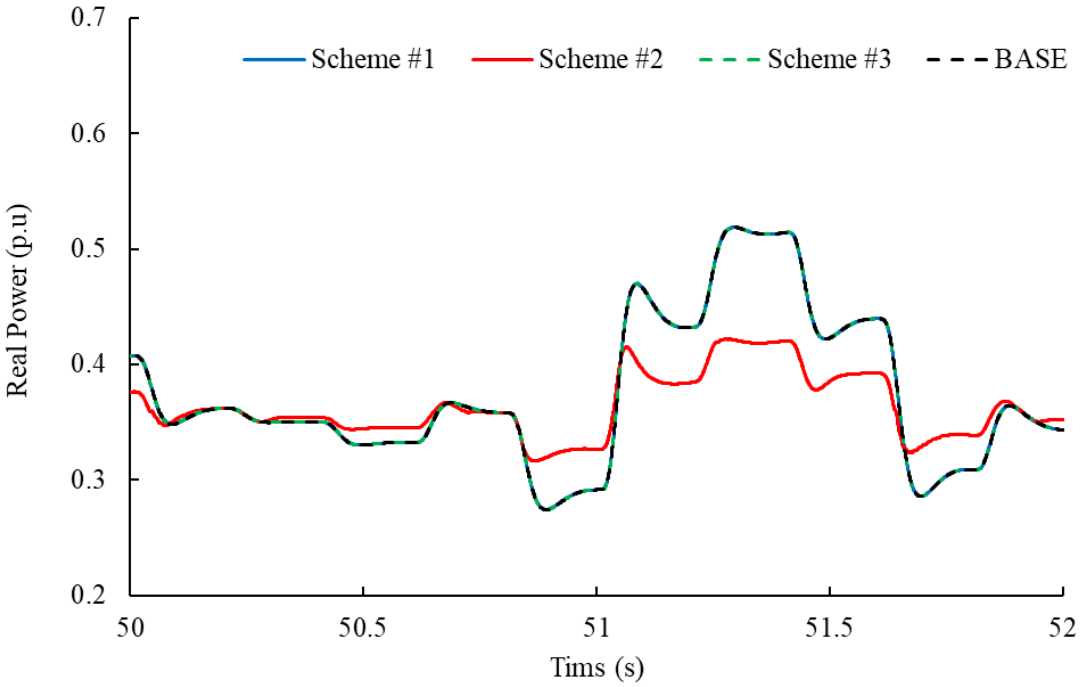

(b) Real power outputs of each control scheme

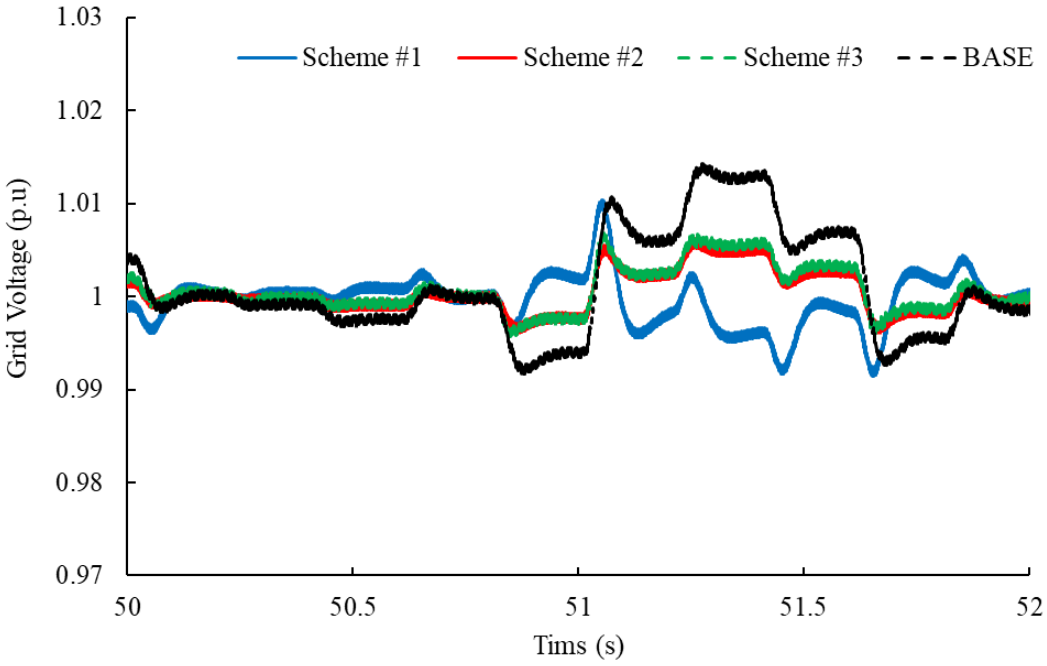

(c) Grid voltage outputs of each control scheme

Figure 4.5. Simulation results for each control scheme when %TI = 7.2%

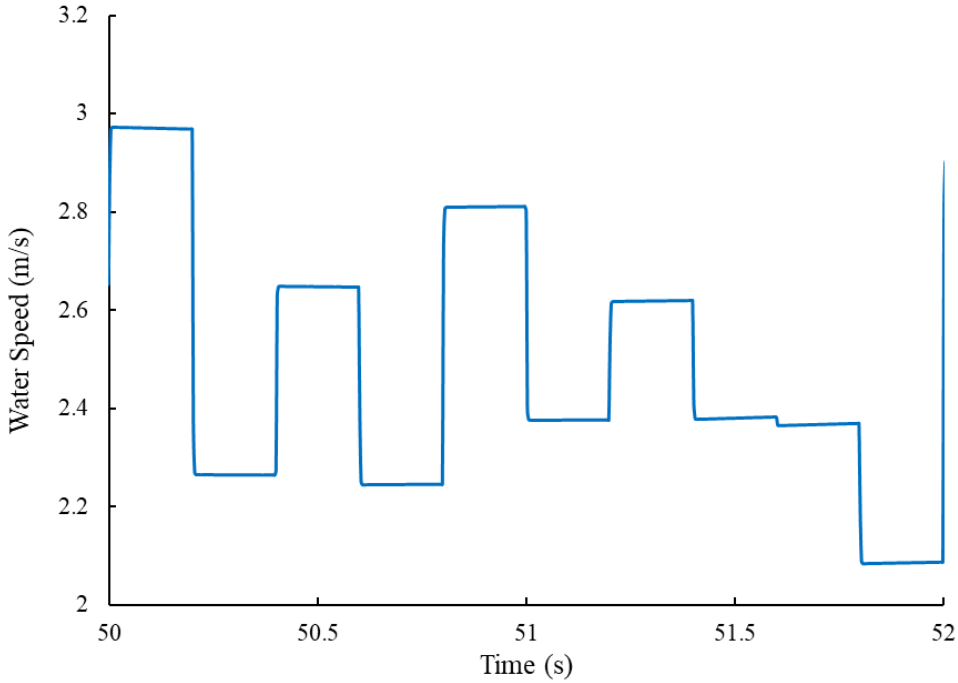

(a) Water speed with %TI = 11.6%

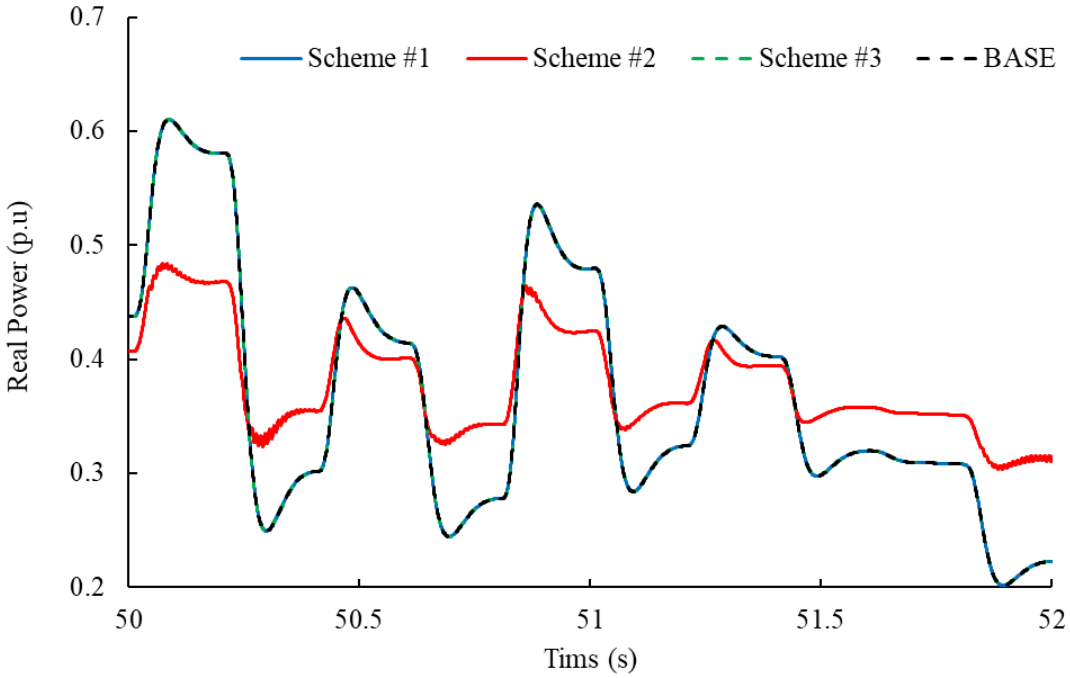

(b) Real power outputs of each control scheme

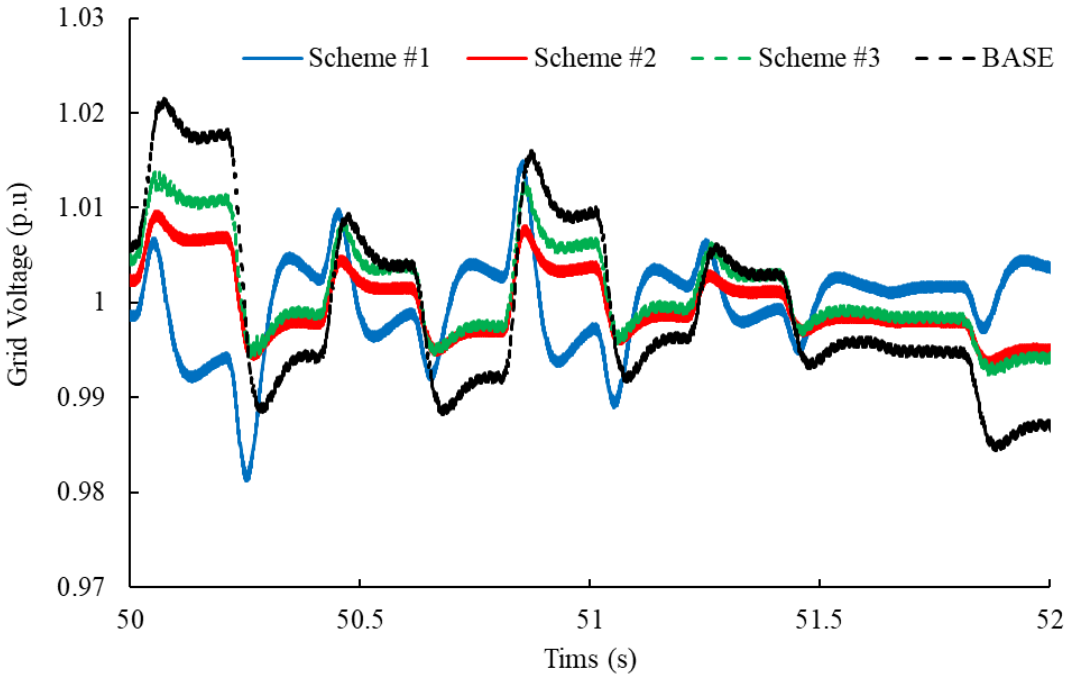

(c) Grid voltage outputs of each control scheme

Figure 4.6. Simulation results for each control scheme when %TI = 11.6%

As shown in Figures 4.5 and 4.6, the real power fluctuation and grid voltage fluctuation become more severe as the water turbulence intensity becomes greater. Therefore, water turbulence also should be considered when flicker mitigation techniques are determined. Since the graphs of the grid voltage in Figures 4.5 and 4.6 cannot be objectively assessed to compare the effectiveness of mitigating flicker for each control scheme, the short-term flicker severity P_{st} is calculated again, and the results of P_{st} for each control scheme with the varied turbulence intensity are shown in Table 4. Figure 4.7 demonstrates the bar graphs of the summary for the results in Table 4 to explain the results intuitively.

Table 4. P_{st} with different turbulence intensity

SCR = 6 & X/R Ratio = 2			
Control	P_{st} (%TI = 3.2%) (Moderate)	P_{st} (%TI = 7.2%) (Severe)	P_{st} (%TI = 11.6%) (Very Severe)
Base	0.6027	1.1228	1.9020
VAR	0.4572	0.9931	1.6456
BESS	0.3576	0.5229	0.6894
Adaptive	0.3968	0.6685	1.0196

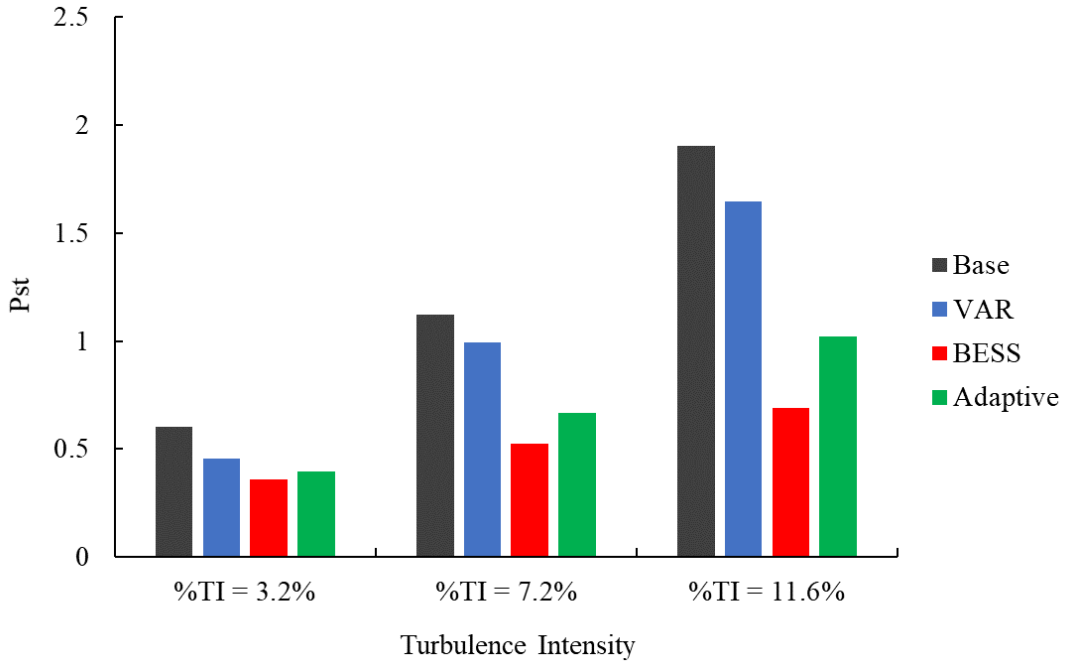

Figure 4.7. Summary of the results in case 2

Considering the limiting value for the acceptable P_{st} on the grid that is $P_{st} = 1.0$, when the turbulence intensity of the water flow is very severe, the voltage fluctuation is mainly caused by the fluctuation of the real power. The very severe turbulence intensity (i.e., %TI = 11.6% in the case study), of course, is unlikely to happen in the river and sea because the turbulence intensity of the water flow in the river is not easily changed; however, with consideration of the worst water turbulence situation, the BESS, which smooths the real power fluctuation out of the tidal power generator (by discharging and charging the amount of the fluctuating real power), might be the best way to mitigate flicker and satisfy the grid code in the area that the tidal power plant is installed. The adaptive control is advantageous to mitigate flicker when the water turbulence is moderate or severe, and it does not require extra cost for implementation of the additional hardware into the system, unlike the BESS. Since the size of the GSC (rated currents of the IGBTs) is limited in the simulation, the simulation results also reflect the limit of flicker mitigation when the water turbulence is very severe, meaning that the reactive current I_q needs more to be injected into the system. Reactive power compensation is easy to implement, but it is limited to mitigate flicker when the X/R ratio of the grid is too low. Therefore, based on grid conditions and the water flow characteristics in the areas where the tidal power plant is installed and the budget, the control scheme of flicker mitigation should be decided. Eventually, the tidal power plant can be integrated into the system by promising the stabilized grid voltage and improved power quality.

5. Conclusion and Future Work

5.1 Conclusion

This thesis proposes a tidal and river MHK power generation model to study the effect of the operational condition of hydrokinetic power (i.e., water turbulence intensity) and grid parameters (i.e., SCR & X/R ratio) on flicker, and to explore the three different control schemes (i.e., reactive power control, use of the BESS, and adaptive $I_q - V$ control) to provide flicker mitigation. The case study and the simulation modeling are performed by PSCAD, which is a dynamic power system software. In order to objectively assess flicker severity in each control scheme and quantify the level of flicker severity, the short-term flicker severity P_{st} is calculated by the flickermeter tool in MATLAB/SIMULINK.

In the theoretical model of the MHK power generation for the digital simulation, the modeling of the PMSG and the hydrokinetic turbine is described, and their mathematical model and MPPT control of the hydrokinetic turbine are explained. The output results of the machine side (PMSG and hydrokinetic turbine) based on the variable water speed are shown in the graph. Then, the electrical power conversion throughout the back-to-back power converter consisting of the diode rectifier, DC-DC boost converter, and DC-AC inverter and their control schemes are described in Chapter 2.4. Based on the theoretical model of the MHK power generation, the three

different control schemes for flicker mitigation are implemented on the system model, and the case studies with the varied water turbulence and varied grid parameters are conducted.

According to the results in the first case study, the BESS and adaptive control effectively mitigate flicker regardless of the X/R ratio, but the VAR control can mitigate flicker only at a certain level of X/R ratio in the weak grid. In the second case study, the real power fluctuation becomes varied by changes in the water turbulence; the BESS that smooths real power fluctuation has the most effective results, and the other two control techniques that use the reactive components have a limit to mitigate flicker when the water turbulence is too severe. As previously mentioned, the implementation of the dedicated storage to the power system is less financially viable than implementing the control logic into the converters; however, in the case of the distribution network with the very weak power system and very severe water turbulence (low impedance angle and very weak grid condition), the BESS can be an adequate decision to mitigate flicker in the tidal and river power generation. But, in the case of the weak grid conditions and severe water turbulence, the adaptive control is the optimal choice to stabilize the voltage fluctuation since it does not require the extra cost and space for implementation, unlike the BESS. Of course, the current capacity (rated current) of the inverters in GSC should be considered when the hydrokinetic system is built. If the distribution network has slightly weak and relatively high X/R ratio, such as distribution network that has a long radial power line, the VAR control in GSC is enough to be used to stabilize the grid voltage and flicker, but the line resistance and line reactance of the grid system must be known when the VAR control is used. Therefore, the mitigation techniques shall be considered based on the types of the grid connection and the water flow characteristics in the areas where the tidal power plant is installed, considering the cost.

5.2 Future Work

The hardware design for verification of the software simulation will be presented in Appendix 1. The main objective of the hardware simulation is to reproduce the hydrokinetic dynamic behavior with the MHK power system and verify the results of the digital simulation. The connection overview of the hardware design will be provided, and the basic model of the induction motor with the VFD, which represents the hydrokinetic turbine, will be explained. Only the induction motor with the VFD and synchronous generator connected to the induction motor with the mechanical shaft are set up now; hence, the rest of the hardware parts such as a microcontroller and power converters to the grid will be handled as future work. The details of the hardware design of the MHK power system that has been completed and will be completed are presented in Appendix 1.

References

[1] M. Mason, “Renewable energy: All you need to know,” *Esyoh, LLC*, 9 November 2016. [Online]. Available: https://www.environmentalscience.org/renewable-energy. [Accessed: 16 June 2020]

[2] E. Muljadi, A. Wright, V. Gevorgian, J. Donegan, C. Marnagh, and J. McEntee, “Power generation for river and tidal generators,” *National Renewable Energy Laboratory (NREL).* [Online]. Available: http://www.nrel.gov/docs/fy16osti/66097.pdf. [Accessed: 16 June 2020]

[3] “Data and Statistics,” *International Energy Agency (IEA),* 12 April 2018. [Online]. Available: https://www.iea.org/data-and-statistics. [Accessed: 16 June 2020].

[4] K. Kilcher, R. Thresher, H. Tinnesand, “Marine Hydrokinetic Energy Site Identification and Ranking Methodology Part I: Tidal Energy,” *National Renewable Energy Laboratory (NREL),* Golden, CO, USA, 2016.

[5] A. Owen, M.L. Trevor, “Tidal Current Energy: Origins and Challenges,” in *Future Energy,* pp. 111-128, 2008.

[6] R. A.R. Tricker, P. Groen, “Tide,” *Encyclopædia Britannica*, 20 February 2020. [Online]. Available: https://www.britannica.com/science/tide. [Accessed: 16 June 2020].

[7] H. J. Yadav, “Recent developments of Ocean Energy in India – An Overview,” in *International Journal on Recent and Innovation Trends in Computing and Communication*, vol. 3, no. 12, pp. 6717 - 6721, Dec. 2015.

[8] “IEEE Recommended Practice for the Analysis of Fluctuating Installations on Power Systems," in *IEEE Std 1453-2015 (Revision of IEEE Std 1453-2011),* vol., no., pp.1-74, 30 Oct. 2015.

[9] C. V. Moreno, H. A. Duarte, and J. U. Garcia, "Propagation of flicker in electric power networks due to wind energy conversions systems," in *IEEE Transactions on Energy Conversion*, vol. 17, no. 2, pp. 267-272, June 2002.

[10] A. Baggini, “Handbook of Power Quality,” New York: Wiley, 2008.

[11] “Electromagnetic Compatibility (EMC)-Part 4: Testing and Measurement Techniques-Section 15: Flickermeter – Functional and Design Specifications,” in *IEC Std. 61000-4-15,* November 1997.

[12] J. C. Gomez and M. M. Morcos, "Flicker Measurement and Light Effect," in *IEEE Power Engineering Review*, vol. 22, no. 11, pp. 11-15, Nov. 2002.

[13] J. MacEnri, M. Reed, and T. Thiringer, "Influence of Tidal Parameters on SeaGen Flicker Performance," *European Wave and Tidal Energy Conference (EWTEC)*, Southampton, UK, 2011.

[14] S. Walker and L. Cappietti, "Experimental Studies of Turbulent Intensity around a Tidal Turbine Support Structure," *Energies*, vol. 10, pp. 497, 2017.

[15] W. Hu, Z. Chen, Y. Wang, and Z. Wang, "Flicker mitigation by active power control of variable-speed wind turbines with full-scale back-to-back power converters," in *IEEE Trans. Energy Convers.*, vol. 24, no. 3, pp. 640–649, Sep. 2009.

[16] M. Ammar and G. Joos, "A short-term energy storage system for voltage quality improvement in distributed wind power," *IEEE Trans. Energy Convers.*, vol. 28, no. 2, pp. 425–433, Dec. 2014.

[17] F. Diaz-Gonzalez, F. Bianchi, A. Sumper, and O. Gomis-Bellmunt, "Control of a flywheel energy storage system for power smoothing in wind power plants," *IEEE Trans. Energy Convers.*, vol. 29, no. 1, pp. 204–214, Mar. 2014.

[18] M. Ammar and M. E. Ammar, "Enhanced Flicker Mitigation in DFIG-Based Distributed Generation of Wind Power," in *IEEE Transactions on Industrial Informatics*, vol. 12, no. 6, pp. 2041-2049, Dec. 2016.

[19] M. Ammar and G. Joos, "Impact of distributed wind generators reactive power behavior on flicker severity," *IEEE Trans. Energy Convers*., vol. 28, no. 2, pp. 425–433, Jun. 2013.

[20] T. L. Van, T. H. Nguyen and D. Lee, "Flicker mitigation in DFIG wind turbine systems," *Proceedings of the 2011 14th European Conference on Power Electronics and Applications*, Birmingham, U.K., pp. 1-10, 2011.

[21] Y. Jiang, M. F. Rong and L. Y. Hua, "Variable speed constant frequency tidal current energy generation and control strategy for maximum power point tracking and grid connection," *2009 International Conference on Sustainable Power Generation and Supply*, Nanjing, China, pp. 1-6, 2009.

[22] M. J. Khan, T. Iqbal, and J. E. Quaicoe, "River current energy conversion systems: Progress, Prospects and Challenges," *Renewable and Sustainable Energy Reviews*. 2008.

[23] *Ocean Renewable Power Company*, [Online]. Available: https://www.orpc.co. Portland, Maine. [Accessed: 20 June 2020]

[24] N. Goudarzi and D. Zhu, "A review on the development of wind turbine generators across the world," *International Journal of Dynamics and Control*, vol. 1, pp. 192-202, 2013.

[25] M. Liu, “Hydrokinetic turbine power converter and controller system design and implementation,” Master Thesis, Vancouver, Canada: University of British Columbia, Aug. 2014.

[26] P.M. Anderson and A.A. Fouad, “Power System Control and Stability,” Piscataway, N.J.: IEEE Press; Wiley-Interscience, 2003.

[27] J. Khan, “A generic performance curve for tidal and hydrokinetic devices,” *Journal of Ocean Technology*, vol. 13. pp. 54-62, 2018.

[28] Y. Song, Y. Chen, S. Huang, Z. Yu and Y. Qiao, "Average value model of grid side converter in PMSG for system-level studies," in *The Journal of Engineering*, vol. 2017, no. 13, pp. 1799-1803, 2017.

[29] G. Shi, M. Zhu, X. Cai, Z. Wang, and L. Yao, "Generalized average model of DC wind turbine with consideration of electromechanical transients," *IECON 2013 - 39th Annual Conference of the IEEE Industrial Electronics Society*, Vienna, pp. 1638-1643, 2013.

[30] T. Sun, Z. Chen, and F. Blaabjerg, "Flicker study on variable speed wind turbines with doubly fed induction generators," in *IEEE Transactions on Energy Conversion*, vol. 20, no. 4, pp. 896-905, Dec. 2005.

[31]Y. Song, Y. Chen, S. Huang, Z. Yu and Y. Qiao, "Average value model of grid side converter in PMSG for system-level studies," in *The Journal of Engineering*, vol. 2017, no. 13, pp. 1799-1803, 2017.

[32] A. Burke, H. Zhao, "Applications of Supercapacitors in Electric and Hybrid Vehicles," *Research Report - UCD-ITS-RR-15–09*, vol. 15, 2015.

[33] A. Vassallo, P. Maker, T. Dixon, and V. Agelidis, "Electricity Storage: Renewable Energy Applications in the Australian Context," in *IEEE Electrification Magazine*, vol. 3, no. 3, pp. 22-29, Sept. 2015.

[34] H. Hesse, M. Schimpe, D. Kucevic, and A. Jossen, “Lithium-Ion Battery Storage for the Grid—A Review of Stationary Battery Storage System Design Tailored for Applications in Modern Power Grids,” *Energies*, vol. 10, pp. 2107, 2017.

[35] O. Tremblay and L. A. Dessaint, “Experimental Validation of a Battery Dynamic Model for EV Applications,” *World Electric Vehicle Journal*, vol. 3, pp. 289-298, 2009.

[36] J. Kim, E. Muljadi, J. Park and Y. C. Kang, "Flexible IQ–V Scheme of a DFIG for Rapid Voltage Regulation of a Wind Power Plant," in *IEEE Transactions on Industrial Electronics*, vol. 64, no. 11, pp. 8832-8842, Nov. 2017.

[37] J. D. Lavers and P. P. Biringer, "Real-Time Measurement of Electric Arc-Furnace Disturbances and Parameter Variations," *in IEEE Transactions on Industry Applications*, vol. IA-22, no. 4, pp. 568-577, July 1986.

[38] N. P. W. Strachan and D. Jovcic, "Stability of a Variable-Speed Permanent Magnet Wind Generator With Weak AC Grids," in *IEEE Transactions on Power Delivery*, vol. 25, no. 4, pp. 2779-2788, Oct. 2010

[39] “IEEE Guide--Adoption of IEC/TR 61000-3-7:2008, Electromagnetic compatibility (EMC)--Limits--Assessment of emission limits for the connection of fluctuating installations to MV, HV and EHV power systems," in *IEEE Std 1453.1-2012 (Adoption of IEC/TR 61000-3-7:2008)*, vol., no., pp.1-78, 6 July 2012.

[40] P.C. Sen, “Principles of electric machines and power electronics,” Chichester, England: John Wiley & Sons, 1997.

Appendix 1. Future Work - Hardware Simulation for Verification

In Appendix 1, the hardware model and emulation for the hydrokinetic power generation are presented. The main objective of the hardware simulation is to reproduce the hydrokinetic dynamic behavior implemented in the microcontroller sending the reference speed to the Variable Frequency Drive (VFD), and the VFD connected to the wound rotor induction motor emulates the variable speed of the tidal turbine. Then, the induction motor that mimics the tidal turbine is connected to the synchronous generator to provide the electrical energy to the grid system. As soon as the hardware simulation is ready to be set up, the verification of the software simulation will proceed to compare the results of the hardware simulation manipulating the voltage flicker on the grid system with the software simulation as future work. Figure A.1 demonstrates the overview of the hardware connection for emulating the hydrokinetic power generation.

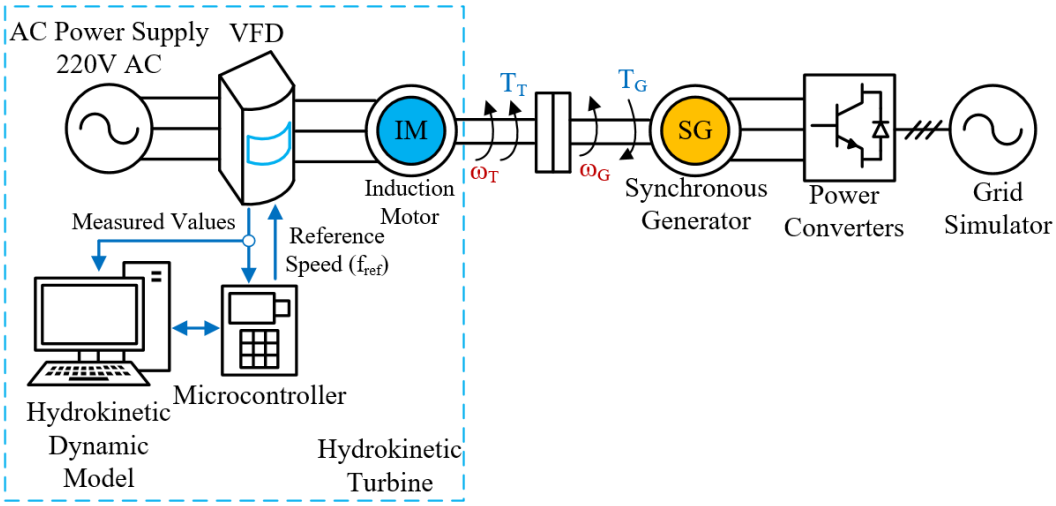

Figure A.1. Connection overview of the hardware simulation

As shown in Figure A.1, the VFD will control the speed of the induction motor based on the hydrokinetic dynamic model on the interface (i.e., PC), and the microcontroller transmits the reference speed to the VFD as an analog signal. The microcontroller helps to exchanges the analog and digital signal between the interface and the hardware such as VFD and motor; it collects analog signals from the motor or power converters and uses them to calculate the reference speed for VFD to emulate the variable speed of the induction motor, which mimics the hydrokinetic turbine. With the given tidal turbine parameters and the specified water speed, the software interface provides the corresponding reference speed for the induction motor throughout the VFD control to emulate the tidal turbine. The next subsection explains the set-up for the induction motor connected to the VFD and the control scheme of the VFD to enable the induction motor operating in the variable speed. Until now, the only induction motor and VFD are tested to operate them as a variable speed motor, and the microcontroller, synchronous generator, and power converters with the grid simulator will be set up as future work in this report. Table 5 indicates the specification of the hardware components that will be used in the hardware simulation. The circuit parameters (resistance and inductance of stator and rotor) of the induction motor are not listed in the table because their values are not indicated on the nameplate, and the manual for the machine does not exist (the model is too old to find the manual). Therefore, the no-load test and blocked-rotor test are required to find the circuit parameters of the induction motor later on.

Table 5. Specification of hardware simulation

Induction Motor	
Horsepower	10 HP
Rated Power	7.457 kW
Rate Speed	1735 RPM
Number of Pole Pairs	2
Input Voltage (Y-Δ)	230 (Low) / 460 (High) V
Rated Current	30 (Low) / 15 (High) A
Frequency	60 Hz
Synchronous Generator	
Rated Power	7.5 kW
Rated Frequency	60 Hz
Power Factor	0.8
Rated Speed	1800 RPM
Voltage	240 (Low) / 480 (High) V
Rated Current	23 (Low) / 11 (High) V
VFD	
Input Voltage	$220 \pm 15\%$ V_{ac}
Output Voltage	0 ~ Rated Input Voltage
Input Frequency	47 ~ 63 Hz
Output Frequency	0 ~ 400 Hz
Rated Power	7.5 kW
Rated Output Current	34 A

Instead of building the real hydrokinetic turbine with the water flow, the variable speed of the induction motor controlled by the VFD will emulate the hydrokinetic turbine in this hardware simulation. The picture of the induction motor connected to the VFD and synchronous generator in the power laboratory is shown in Figure A.2.

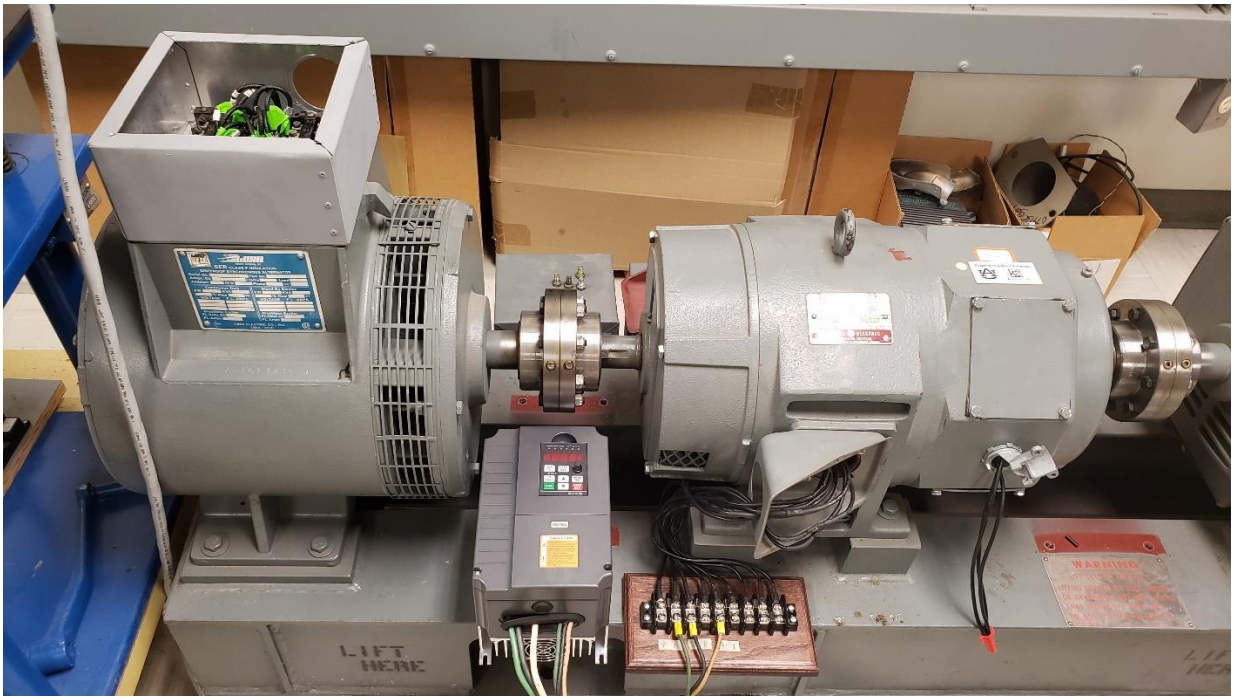

Figure A.2. Picture of the induction motor, synchronous generator, and VFD

Before presenting the VFD functionality, the characteristics of the induction motor and its speed control with the V/F control implemented in the VFD should be explained to understand the control scheme of the VFD. It is essential to understand the characteristics of the induction motor in order to explain the use of the VFD that makes the induction motor emulating the hydrokinetic turbine as a variable speed drive. The equivalent circuit of the induction motor is shown in Figure A.3.

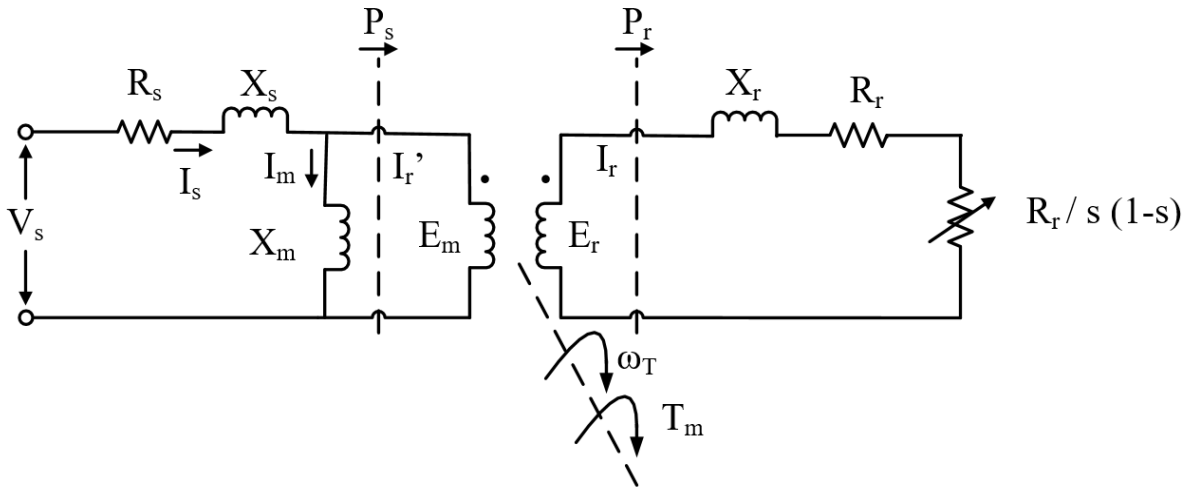

Figure A.3. Equivalent circuit of the induction machine

The induction machine, or asynchronous machine, has a stator side and a rotor side, mainly. Both stator winding and rotor winding carry alternating currents, and the AC is supplied to the stator winding and rotor winding by induction. The details of the induction machine and its mechanisms are explained in the literature [40]. In this section, the basic derived equations for the running operation in the induction machine and the speed control for the induction motor are presented. Referencing to Figure A.3, if the stator windings are connected to a three-phase supply (VFD in this simulation), and the rotor circuit is closed, the induced voltages in the rotor side produce the rotor currents. These rotor currents interact with the air gap field to produce the torque, and then the rotor starts rotating because of the relative speed difference between the rotating field and the rotor winding. In the induction machine, there are no induced voltages, currents, and torques at $n_r = n_{sync}$. Therefore, the slip *s* that is the difference between n_r and n_{sync} is a very significant factor in understanding the running operation of the induction machine, and the slip is defined as:

$$s = \frac{n_{sync} - n_r}{n_{sync}} \qquad (A.1)$$

Therefore, in order to rotate the rotor of the induction motor, the slip should be greater or less than 0 instead of being equal to zero ($n_r = n_{sync}$). The relative speed between the rotating field and the rotor winding should exist to rotate the machine in the induction motor. Then, the slip frequency f_r of the induced voltage and the current in the rotor circuit will correspond to this slip rpm ($n_{sync} - n_r = s\ n_{sync}$) because this is the relative speed between the rotating field and the rotor winding. The rotor circuit frequency f_r can be written as:

$$f_r = \frac{p}{120}\left(n_{sync} - n_r\right) = \frac{p}{120} s n_{sync} = s f_s \qquad (A.2)$$

where p is the number of poles, and f_s is the stator circuit frequency (frequency of the supply). Then, the induced currents in the rotor windings also produce a rotating field, and its speed in RPM with respect to the rotor (represent the speed of the motor, usually) is:

$$n = 120 * \frac{f_r}{p} = 120 * \frac{s f_s}{p} = s\ n_{sync} \qquad (A.3)$$

Unlike the synchronous generator, as explained in chapter 2.3, the induction motor has a slip, and the slip is an important factor in expressing the speed of the induction machine.

As shown in Figure A.3, the equivalent circuit of the induction motor consists of the stator winding part and rotor winding part. In Figure A.3, the stator winding can be represented, where:

V_s = per-phase terminal voltage in stator side

R_s = per-phase stator winding resistance

X_s = per-phase stator leakage inductance

X_m = per-phase stator magnetizing inductance

E_m = per-phase induced voltage in the stator winding

And, the rotor winding can be represented in Figure A.3, where:

E_r = per-phase induced voltage in the rotor

R_r = per-phase rotor circuit resistance

X_r = per-phase rotor leakage inductance

On the rotor side equivalent circuit, R_r (1-s)/s represents the speed-dependent resistance that represents the mechanical power developed by the induction motor; therefore, the mechanical power can be represented as:

$$P_{mech} = I_r^2 \frac{R_r}{s} (1 - s) = (1 - s) P_{airgap} \qquad (A.4)$$

where P_{airgap} is the power that crosses the air gap.

Now, the basic operation concept and equations for the induction machine have been represented. With this operating concept of the induction machine, the VFD that controls the frequency and the voltage of the AC supply on the stator side to reproduce the variable speed will be explained. The synchronous speed can be varied by changing the frequency of the supply to change the motor speed. In the VFD, the constant V/f control is imbedded to vary the frequency of the supply. In order to understand V/f control, the equation of the motor flux Φ_k should be considered:

$$\Phi_k = E_m / f$$

where E is the induced voltage on the stator winding, and f is the frequency of the supply. Since the voltage drop across R_s and X_s is small compared to the terminal voltage of the stator side V_s, so $V_s = E_m$ So, the motor flux can be rewritten as:

$$\Phi_k = V/f$$

Therefore, in order to change the speed, the terminal voltage of the motor is varied as the frequency of the supply changes proportionally. This control is called "constant volts per hertz."

To maintain the constant air gap flux density, the required variation of the supply voltage with the frequency should exist, as shown in Figure A.4.

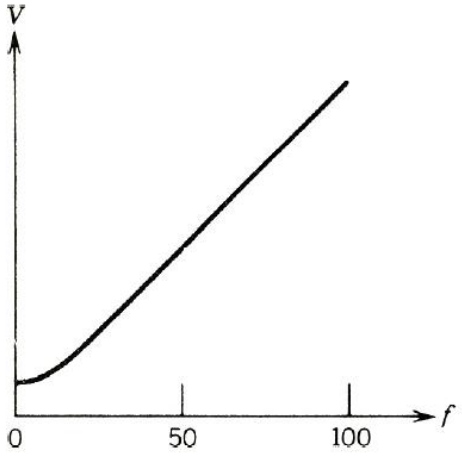

Figure A.4. V/f pattern for the constant volts per hertz control in the induction machine

With this V/f control, the VFD control scheme is shown in Figure A.5 with the hydrokinetic dynamic model.

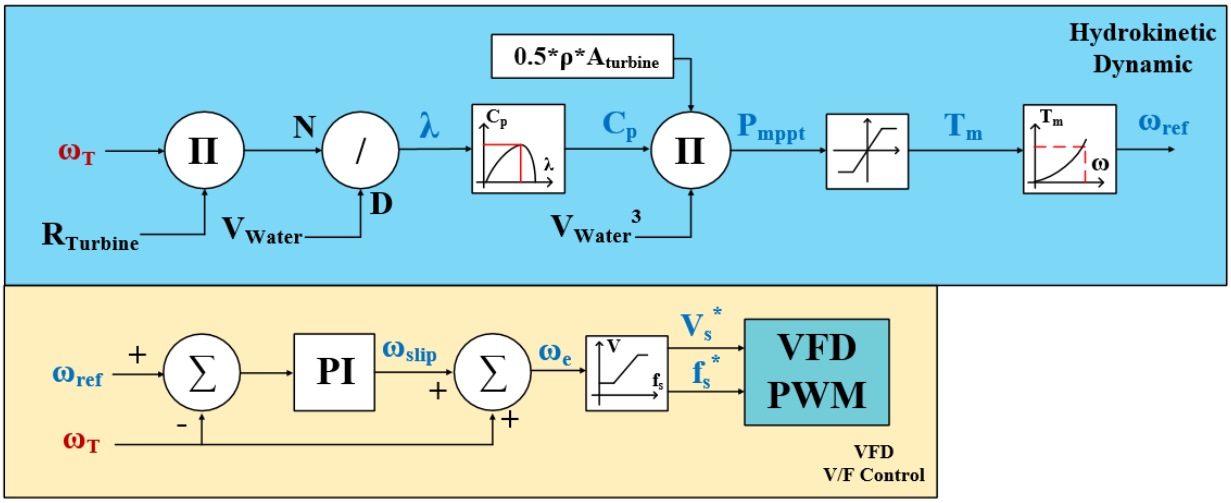

Figure A.5. VFD control scheme with hydrokinetic dynamics

In Figure A.5, the hydrokinetic dynamics are already explained in the previous chapter 2.3; the VFD requires the reference frequency in proportion to the voltage representing the corresponding reference speed obtained from the hydrokinetic dynamics. ω_e represents the reference synchronous speed obtained from the reference speed of the turbine (ω_{ref}) from the MPPT of the hydrokinetic dynamic. Therefore, the induction motor operates in the reference frequency based on the reference speed of the hydrokinetic dynamics. The induction motor emulates the hydrokinetic turbine following the hydrokinetic dynamics embedded in the interface (i.e., PC and microcontroller). Figure A.6 also demonstrates the VFD equivalent circuit with the connected AC source and the induction motor. As shown in Figure A.6, the topology for the VFD circuit is very similar to the back-to-back converter; the AC source is converted to the DC throughout the diode rectifier (AC-DC), and the PWM control signals for the VFD control as shown in Figure A.5 are carried to the inverters on the right side to control the speed of the induction machine throughout the DC-AC inverter. The control circuit for generating the PWM is embedded in the VFD. Therefore, the VFD controls the input frequency and the voltage of the

induction motor in order to control the motor speed, eventually. So, the induction motor controlled by the VFD can emulate the tidal turbine, including the hydrokinetic dynamics, according to the above explanation.

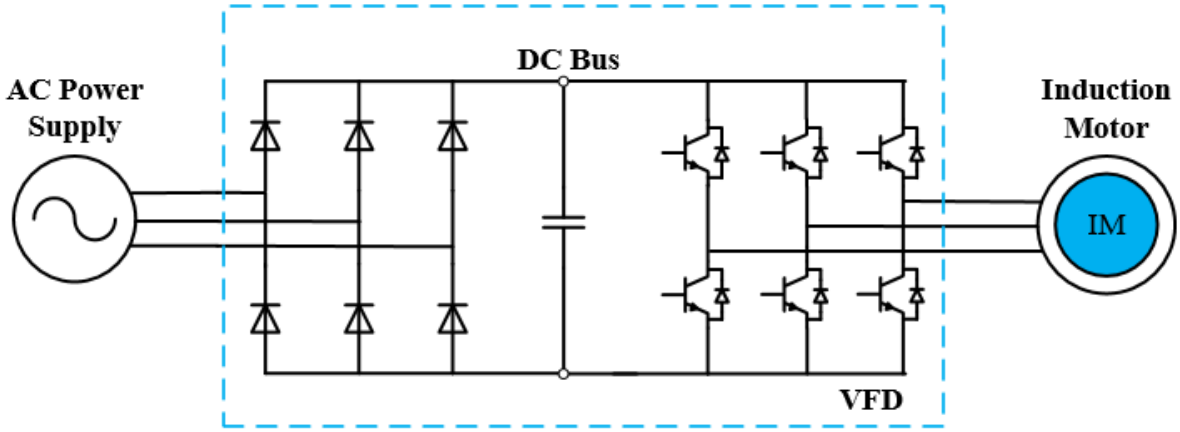

Figure A.6. The equivalent circuit for the VFD connected to the induction motor

Then, the induction motor controlled by the VFD is directly connected to the synchronous generator with the shaft coupling (mechanically direct coupled), and its mechanical coupling reflects the equation of the mechanical model in equation (2.13).

The hardware design that is set up now is the induction motor with the VFD and synchronous generator connected to the induction motor. The rest of the system will be discussed in future work.

For the hardware simulation, the only tidal turbine (induction motor and VFD) part is operated and tested. The synchronous generator is connected to the induction motor with direct shaft coupling. However, the power converters connection and grid system simulator are not set up yet. According to the software model of the hydrokinetic power generation, the power converter should consist of:

1. The AC-DC diode rectifier to convert the variable AC of the synchronous generator into the variable DC.

2. The DC-DC converter to control the DC voltage, maintaining the output power based on the MPPT control.

3. The DC-AC inverter to implement the GSC controls or the corresponding flicker mitigation control schemes and DC-link constant.

Then, the grid simulator existed in the power laboratory (NHR - 9410 model) will be connected to the output of the DC-AC inverter, so the hardware system can operate as similar to the digital simulation and verify the results obtained from the digital simulation.